Physica D 454 (2023) 133880

Contents lists available at ScienceDirect

Physica D

journal homepage: www.elsevier.com/locate/physd

On the Arctic Amplification of surface warming in a conceptual climate model

Philip Goodwin [a,*], Richard G. Williams [b]

[a] School of Ocean and Earth Science, University of Southampton, Southampton, UK
[b] School of Environmental Science, University of Liverpool, UK

ARTICLE INFO

Article history:
Received 29 January 2023
Received in revised form 17 July 2023
Accepted 2 August 2023
Available online 9 August 2023
Communicated by Dmitry Pelinovsky

Dataset link: https://doi.org/10.5281/zenodo.8151916, https://crudata.uea.ac.uk/cru/data/temperature/, https://www.metoffice.gov.uk/hadobs/hadcrut5/data/current/download.html, https://ceres.larc.nasa.gov/data/, https://doi.org/10.24381/cds.68653055

Keywords:
Arctic amplification
Polar amplification
Energy balance climate models
Conceptual climate modelling

ABSTRACT

Over the last century Earth's surface temperatures have warmed by order 1 K as a global average, but with significant variation in latitude: there has been most surface warming at high Northern latitudes, around 3 times more than in low latitude regions (termed Arctic Amplification), while there has been least warming over the Southern Ocean. Many contributing processes have been suggested to explain this asymmetrical latitudinal warming pattern, but quantification of the contributing factors responsible remains elusive. Complex general circulation climate models can reproduce similar asymmetrical patterns of warming, but it can be difficult to interpret the contributing processes. Meanwhile, idealised conceptual energy balance climate models have been able to reproduce a general polar amplification of warming whose origins can be interpreted, but this warming is often symmetrical across both hemispheres and may not be responsible for the real-world pattern. Here, we use a conceptual Energy Balance Model, with imposed closures for initial horizontal diffusivity and cloudiness drawing upon observational constraints and including temperature-dependent diffusivity and a sub-surface ocean heat reservoir, to show that the magnitude of present-day Arctic Amplification may arise through relatively simple thermodynamic (Clausius–Clapeyron) and radiative (climate feedback) processes. The current asymmetry between hemispheric warming may arise due to the transient heat transport up through the base of the surface ocean mixed layer from the slow-responding deep ocean to the fast-responding surface ocean being dominated by upwelling in the Southern Ocean. It should be noted that the processes identified here are not a unique in offering a potential solution, and so significant, or dominant, roles for dynamical processes remain plausible explanations for Arctic Amplification.

1. Introduction

The current period of climate change is characterised by rising surface temperatures driven by anthropogenic emission of greenhouse gasses [1], with the global and annual mean surface temperature having so far risen by order 1 K since the late 19th century. However, the warming has not been evenly distributed with latitude (HadCRUT5, [2]; Fig. 1, black): zonal and annual mean surface temperatures have risen around 3 times more in the Arctic than at the equator over the last hundred years (Fig. 1, black), while zonal and annual average temperatures over the Southern Ocean, at latitudes around 55° to 60° S, have risen less than at the equator.

Earth's climate has undergone many periods of natural climate change in the past, and reconstructions reveal key instances where the change in surface temperatures in Polar regions was greater than in equatorial regions: e.g. the last glacial termination [3] (Fig. 1, red) and the Palaeocene–Eocene Thermal Maximum [4] (Fig. 1, blue). While reconstructions from both periods reveal enhanced warming at high latitudes relative to low latitudes, neither period has the same asymmetrical pattern as the observed warming over the last century (Fig. 1).

The faster observed rate of warming at high Northern latitudes, termed Arctic Amplification, has had many proposed explanations (e.g. [5,6]), which may be acting together. These contributing processes may involve: (i) modifications in vertical radiative balance, such as involving changes in albedo at high latitude as the local temperatures warm due to ice loss; (ii) dynamical features of the atmosphere and/or ocean, such as involving changes in poleward heat transport due to atmosphere and/or ocean circulation changes; or (iii) combined radiative and circulation responses, such as involving changes in albedo due to changes in atmospheric cloud distributions.

This study uses Energy Balance Models (EBMs) to explore possible explanations for the observed latitudinal variation in surface warming (Fig. 1, black). Some previous Energy Balance

* Corresponding author.
E-mail address: p.a.goodwin@soton.ac.uk (P. Goodwin).

https://doi.org/10.1016/j.physd.2023.133880

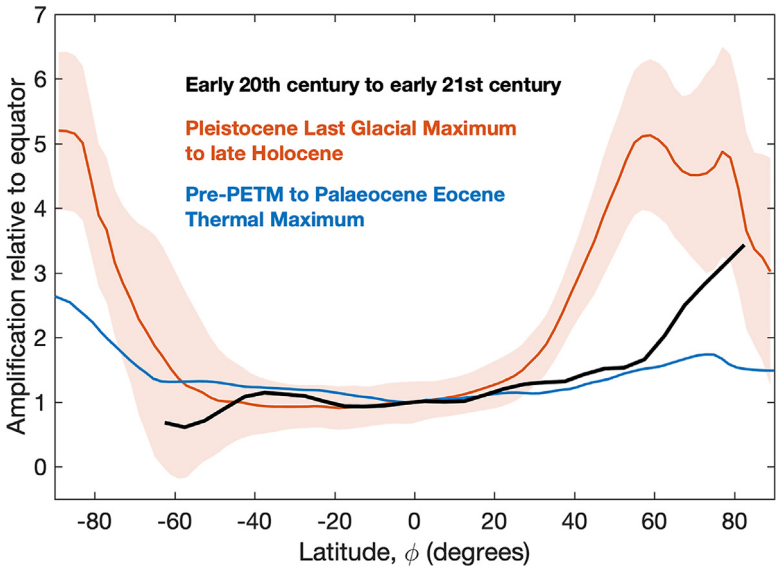

Fig. 1. Reconstructed amplification of surface temperature change with latitude during three periods of global climatic change, expressed relative to equatorial temperature change. Shown are the latitudinal amplification of surface temperature change during: the historic period from 1900–1920 to 2000–2020 from the HadCRUT5 observational reconstruction (Black: [2]); the Pleistocene Last Glacial Maximum to late Holocene (red: [3]) and Palaeocene Eocene Thermal Maximum warming (blue: [4]) from analyses combining geological proxy archives with numerical climate models.

Model studies provide steady-state analytical solutions or approximations (e.g. [7–9]), and rely on simple functional form closures. However, there are difficulties in choosing simple functional forms for key closures in Energy Balance Models, such as the lateral heat diffusivity and cloudiness, which are representing very complex physical processes (see e.g. [10]). Instead of attempting functional form closures for these two quantities, the EBMs presented here impose distributions implied from observations of the recent climate state.

Here, three conceptual energy balance climate models (EBMs) are presented and numerically solved to explore plausible reasons for both the observed Arctic Amplification of warming and the observed reduced warming over the Southern Ocean over the last century (Fig. 1, black). The first model, inspired by classic EBMs (e.g. [8,11,12]), has diffusive poleward heat transport based on dry bulb temperature with diffusivity unaffected by surface warming. The second conceptual EBM presented, inspired by moist static diffusive EBMs (e.g. [9]), has changes in the efficiency of lateral heat transport, represented by lateral diffusivity, with warming to account for changes in the latent to dry energy change as air warms. The third EBM combines the second EBM with a deep ocean heat reservoir, inspired by classic two-box ocean models exploring the impact on transient warming of the large heat capacity deep ocean (e.g. [13]).

In this study, the three presented EBMs are solved numerically by employing a time-stepping scheme to transfer energy horizontally within the surface climate layer and between the surface climate layer and sub-surface ocean with 5° latitudinal resolution (code supplied). This study solves an EBM numerically because: (i) latitudinal variation in observationally constrained lateral diffusivity and cloudiness do not have simple functional forms; (ii) a transient solution is sought in Section 4. The goal is to identify possible causes of the observed Arctic Amplification and relatively damped Southern Ocean warming using a model whose equations are empirically constrained, simple enough to interpret and have enough theoretical justification to provide mechanistic insight.

Next the energy balance of the Earth is described in a global mean and then this approach is generalised to include latitudinal changes in the energy balance.

1.1. Earth's global spatial mean energy balance

The global spatial net heat uptake of the Earth system at the top of the atmosphere (TOA), $\overline{\mathcal{H}}$ in Wm^{-2}, is given by the difference between the incoming solar radiation, $\overline{R_{in}}$ in Wm^{-2}, and the outgoing radiation, $\overline{R_{out}}$ in Wm^{-2},

$$\overline{\mathcal{H}} = \overline{R_{in}} - \overline{R_{out}} \tag{1}$$

where an overbar indicates a global spatial mean value and $\overline{R_{out}}$, depends in some way on Earth's global mean surface temperature, $\overline{T_S}$ in K. A radiative forcing of Earth's climate, $\delta\overline{F}$ in Wm^{-2}, is defined as the change in incoming solar radiation minus the change in outgoing radiation at fixed surface temperature due to some perturbation,

$$\delta\overline{F} = \delta\overline{R_{in}} - \delta\,\overline{R_{out}}\big|_{\delta T=0} \tag{2}$$

where perturbation to outgoing radiation could arise by changing the atmospheric composition, for example release of greenhouse gasses. Initially, with surface temperature held constant, $\delta\overline{T_S} = 0$, the net energy imbalance is equal to the radiative forcing, $\overline{\mathcal{H}} = \delta\overline{F}$. After some time with $\overline{\mathcal{H}} \neq 0$, the energy imbalance alters Earth's surface temperature, $\delta\overline{T_S} \neq 0$, and we have,

$$\overline{\mathcal{H}} = \delta\overline{F} - \delta\,\overline{R_{out}}\big|_{\delta T} = \delta\overline{F} - \overline{\lambda}\delta\overline{T_S} \tag{3}$$

where $\delta\,\overline{R_{out}}\big|_{\delta T}$ (in Wm^{-2}) is the Earth's global mean radiation response from changing surface temperature, and $\overline{\lambda} = \frac{\partial\,\overline{R_{out}}\big|_{\delta T}}{\partial\overline{T}}$ (in $\mathrm{Wm}^{-2}\mathrm{K}^{-1}$) is termed Earth's climate feedback. Eventually, Earth's energy balance is restored, $\overline{\mathcal{H}} \to 0$, as Earth's surface temperature reaches a new steady state value such that,

$$\delta\overline{T_S} = \delta\overline{F}/\overline{\lambda} \tag{4}$$

This feedback response is represented so far in terms of the global-mean response to a temporal perturbation in radiative forcing.

This study considers what determines the latitudinal pattern encapsulated within this global-mean warming response, $\delta\overline{T_S}$, using conceptual energy balance models. These Eqs. (1)–(4) refer to the global-mean energy balance, and global-mean surface

temperature response to radiative forcing. The aim next is to extend this approach and consider an equivalent latitudinal energy balance, so as to address the controls on the latitudinal contrast in warming response to radiative forcing.

Section 2 presents a new conceptual energy balance model, using observational records of Earth's absolute surface temperature [14], top-of-the-atmosphere outgoing radiation under all-sky and clear-sky conditions [15] and cloudiness [16], to constrain the idealised functional relationships governing longwave and shortwave radiation and horizontal heat transport within the model. The model is then forced with incoming solar radiation and the idealised functional relationships within the model reproduce plausible simulations with latitude of Earth's steady-state temperature, radiation budget and horizontal heat transport. Section 3 then perturbs this conceptual EBM first with a dry-atmosphere approximation, finding that Arctic amplification in warming is too small relative to observations. Section 4 perturbs the conceptual EBM secondly with a moist-atmosphere approximation, finding that Arctic amplification is of a similar magnitude to observations, but that Antarctic warming is too high. Section 5 then introduces heat transfer between the surface and deep ocean in the third EBM, and finds that transient warming contains both Arctic amplification and weaker Southern hemisphere warming in similar magnitudes to observations.

2. A conceptual energy balance model inspired by observations

The conceptual EBM presented and used here solves for zonal- and annual-mean surface temperature with latitude. In the EBM the global mean energy balance in Eqs. ((1)–(4)) need to be extended by considering latitudinal variations in the vertical radiation balance, the horizontal heat transport and how the radiative response to radiative forcing perturbations varies with latitude.

2.1. Conceptual energy balance model

This sub-section considers the core vertical and horizontal balances in the model, and how the model is perturbed by radiative forcing.

2.1.1. Vertical radiation budget

The vertical radiation budget is considered separately for three sky-conditions: entirely clear-sky (where there are no clouds), entirely cloudy-sky (where the fraction of area covered by cloud is 1) and all-sky (where the fraction of cloud cover is as the observed climatology). The outgoing radiation at the top-of-the-atmosphere (TOA) under some specified sky-condition i, $R_{out,i}$ in Wm^{-2}, is given by,

$$R_{out,i}(\phi) = L_{out,i}(\phi) + S_{out,i}(\phi) = \varepsilon_i(\phi)\sigma T_S^4(\phi) + \alpha_i(\phi) R_{in}(\phi) \quad (5)$$

where subscript i could indicate either clear-sky, cloudy-sky or all-sky conditions; ϕ is latitude; L_{out} is the outgoing longwave radiation at the top of the atmosphere (TOA); S_{out} is the outgoing shortwave radiation at the TOA; ε is the local emissivity; σ is the Stephan–Boltzmann constant in $\mathrm{Wm}^{-2}\mathrm{K}^{-4}$; T_S is the local surface temperature in K; α is the local albedo; and R_{in} is the local incoming solar radiation in Wm^{-2}. The following sub-sections detail how emissivity, $\varepsilon_i(\phi)$, and albedo, $\alpha_i(\phi)$, are considered in the model for clear-sky, cloudy-sky and all-sky conditions. Note that all quantities are zonal-mean, and there is no seasonality within the conceptual EBM.

2.1.2. Effect of horizontal heat transport

The zonal-mean heating of the system per unit area per unit time, $\mathcal{H}$ in Wm^{-2}, as a function of latitude is then equal to the heat capacity, c in $\mathrm{Jm}^{-2}\mathrm{K}^{-1}$, multiplied by the rate of warming, $\frac{dT_S}{dt}$ in Ks^{-1}, which is equal to the difference between R_{in} and $R_{out,AllSky}$ plus the meridional convergence in the mean northward horizontal heat transport, $-\frac{\partial f}{\partial y}$ in Wm^{-2};

$$\mathcal{H}(\phi) = c(\phi)\frac{dT_S}{dt}(\phi) = R_{in}(\phi) - R_{out,AllSky}(\phi) - \frac{\partial f}{\partial y}(\phi) \quad (6)$$

where at steady state the temperatures stabilise and $\mathcal{H}(\phi) = 0$.

2.1.3. Effect of radiative forcing perturbations on the latitudinal radiative response

A positive radiative forcing to the latitudinal version of Eq. (2), $\delta F(\phi)$ in Wm^{-2}, can arise from the net increase in incoming radiation due to either an increase incoming solar radiation or a decrease in outgoing radiation at constant surface temperature,

$$\delta F(\phi) = \delta R_{in}(\phi) - \delta R_{out}|_{\delta T=0}(\phi) \quad (7)$$

where increasing greenhouse gas concentrations leads to positive $\delta F(\phi)$ through a negative $\delta R_{out}|_{\delta T=0}(\phi)$. Once the climate system has responded to a radiative forcing, a new steady state will eventually be reached whereby $\mathcal{H}(\phi) = 0$ at all latitudes, Eq. (6), with $\delta F(\phi)$ is balanced through a latitudinally-varying combination of the vertical radiative response from rising surface temperatures, $\delta R_{out,AllSky}\big|_{\delta T}(\phi)$, and the change in horizontal heat flux, $\delta\left[\frac{\partial f}{\partial y}\right](\phi)$,

$$\begin{aligned}\delta F(\phi) &= \delta R_{out,AllSky}\big|_{\delta T}(\phi) - \delta\left[\frac{\partial f}{\partial y}\right](\phi)\\ &= \frac{\partial R_{out,AllSky}}{\partial T_S}(\phi)\,\delta T_S(\phi) - \delta\left[\frac{\partial f}{\partial y}\right](\phi)\end{aligned} \quad (8)$$

where $\frac{\partial R_{out,AllSky}}{\partial T}$ in $\mathrm{Wm}^{-2}\mathrm{K}^{-1}$ is equal to the amount of additional outgoing radiation per unit increase in surface temperatures at some latitude. Evaluating from global averages, $\bar{\lambda} = \partial\overline{R_{out,AllSky}}/\partial\overline{T_S}$ gives the climate feedback (Eq. (4); e.g. [1,17]), and so here we refer to the local latitudinal value of $\frac{\partial R_{out,AllSky}}{\partial T}$ as the effective climate feedback with latitude; although note that one cannot simply find the global spatial average of $\frac{\partial R_{out,AllSky}}{\partial T}$ to evaluate the climate feedback since the temperature perturbation is not uniform. This study uses conceptual EBMs to explore why the balancing of a uniform radiative forcing $\delta F(\phi)$, leads to the observed latitudinal variation in surface warming, $\delta T_S(\phi)$. The first two conceptual EBMs consider the eventual steady state response, Eq. (8), while the third considers additional transient terms for heat exchange between the surface ocean and deep ocean.

The conceptual Energy Balance Model solves for the steady state zonal- and annual-mean surface temperature, T_S, with latitude, ϕ, from Eqs. ((5)–(8)) for: imposed incoming zonal-and annual- mean solar radiation with latitude, $R_{in}(\phi)$ in Wm^{-2}; parameterised heat transport with imposed horizontal diffusivity with latitude, $\kappa_{eff}(\phi)$ in $\mathrm{W\,K^{-1}\,m^{-1}}$, and (to account for the differences between clear-sky, cloudy-sky and all-sky conditions) imposed cloudiness with latitude, with $f_{CA}(\phi)$ being the zonal- and annual-cloud amount fraction and $f_{CI}(\phi)$ being the zonal- and annual-mean fraction of incoming shortwave radiation that is incident on clouds. Note that $f_{CA}(\phi)$ and $f_{CI}(\phi)$ differ due to sub-annual variation in both incoming radiation and cloudiness. The imposed fields for $\kappa_{eff}(\phi)$, $f_{CA}(\phi)$ and $f_{CI}(\phi)$ are calculated from observational reconstructions of latitudinal variation in outgoing radiation [15], surface temperatures [14] and cloudiness [16].

The following sub-sections detail the closures for the vertical longwave, shortwave radiation and horizontal heat transport, and

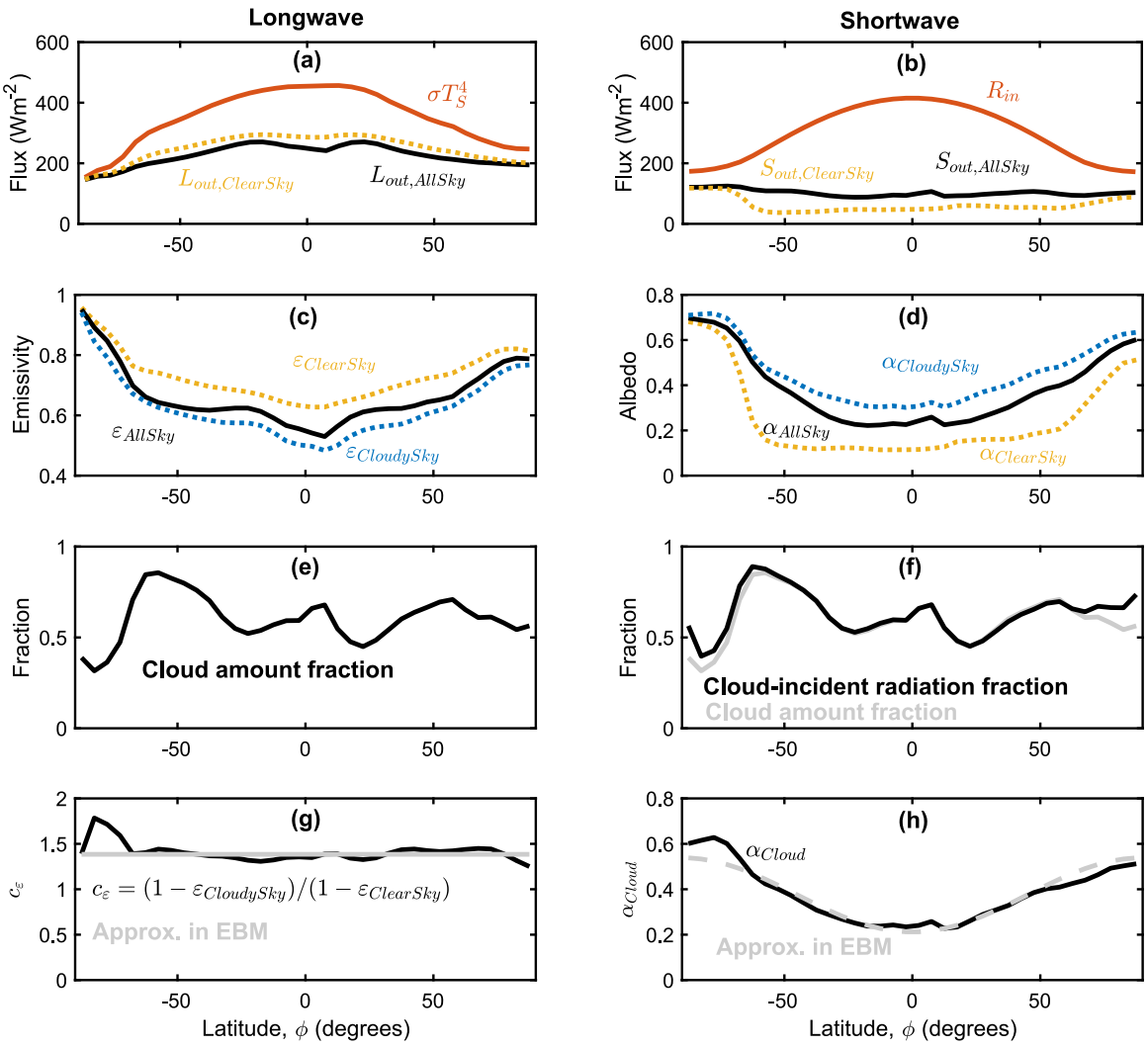

Fig. 2. Annual- and zonal-mean longwave and shortwave radiation budgets, emissivity and albedo with latitude under different sky-conditions, and cloud properties. (a) Outgoing longwave radiation under all-sky, $L_{out,AllSky}$, and clear-sky, $L_{out,ClearSky}$ conditions, along with surface emitted longwave, σT_s^4. (b) Outgoing shortwave radiation budgets, $S_{out,AllSky}$ and $S_{out,ClearSky}$, and incident solar radiation, S_{in}. (c) Emissivity under all-, clear- and cloudy-sky conditions, ε_{AllSky}, $\varepsilon_{ClearSky}$ and $\varepsilon_{CloudySky}$. (d) Albedo under all-, clear- and cloudy-sky conditions, α_{AllSky}, $\alpha_{ClearSky}$ and $\alpha_{CloudySky}$. (e) The cloud amount fraction, f_{CA}. (f) The cloud-incident fraction for solar radiation, f_{CI} and cloud amount fraction, f_{CA}. (g) The ratio of absorptivity of emitted longwave radiation under cloudy-sky conditions relative to clear-sky conditions, c_ε. (h) The calculated albedo of cloud, α_{Cloud}.

how each are calculated within the EBM using selected observational constraints. Many previous Energy Balance Models choose simple closures for outgoing radiation as a function of surface temperature (e.g. [7–9,11]). Here, we consider separate longwave and shortwave balances, and use observations to motivate functional form closures that explicitly calculate the impact of cloudiness on both emissivity and albedo.

2.2. Longwave radiation and emissivity

The annual- and zonal-mean outgoing longwave radiation at latitude ϕ for sky-condition i, $L_{out,i}(\phi)$ in Wm^{-2}, is given by the emissivity of the atmosphere at sky condition i and latitude ϕ, $\varepsilon_i(\phi)$, multiplied by the longwave radiation emitted by the surface at ϕ,

$$L_{out,i}(\phi) = \varepsilon_i(\phi)\,\sigma T_S^4(\phi) \tag{9}$$

where sky-condition i represents either all-sky, clear-sky or cloudy-sky conditions, the Stefan–Boltzmann constant $\sigma = 5.67 \times 10^8$ Wm^{-2}K^{-4} and T_S is the surface temperature in K, with σT_S^4 being the expected emitted longwave radiation at the surface for a black-body.

The climatological annual- and zonal-mean emissivity at latitude ϕ and under sky-condition i, $\varepsilon_i(\phi)$, where i signifies clear sky and all sky conditions are then formally defined as,

$$\varepsilon_i(\phi) = \int_t^{t+n\Delta t} \frac{L_{out,i}(\phi,t')}{\sigma T_S^4(\phi,t')}dt' \Big/ \int_t^{t+n\Delta t} dt' \tag{10}$$

where $n\Delta t$ is an integer number of years and T_S is raised to the 4th power before zonal and temporal averaging.

This relation, Eq. (10), is used to evaluate $\varepsilon_{AllSky}(\phi)$ and $\varepsilon_{ClearSky}(\phi)$ (Fig. 2c, black and orange). The next step is to evaluate cloudy sky emissivity, $\varepsilon_{CloudySky}(\phi)$, which is defined as the emissivity at latitude ϕ when latitudinal cloud amount fraction $f_{CA}(\phi) = 1$. A model closure is adopted where the all-sky emissivity at latitude ϕ, $\varepsilon_{AllSky}(\phi)$, is assumed to be a linear combination of the clear-sky emissivity, $\varepsilon_{ClearSky}(\phi)$, and the emissivity of cloudy-sky, $\varepsilon_{CloudySky}(\phi)$,

$$\varepsilon_{AllSky}(\phi) = [1 - f_{CA}(\phi)]\,\varepsilon_{ClearSky}(\phi) + f_{CA}(\phi)\,\varepsilon_{CloudySky}(\phi) \tag{11}$$

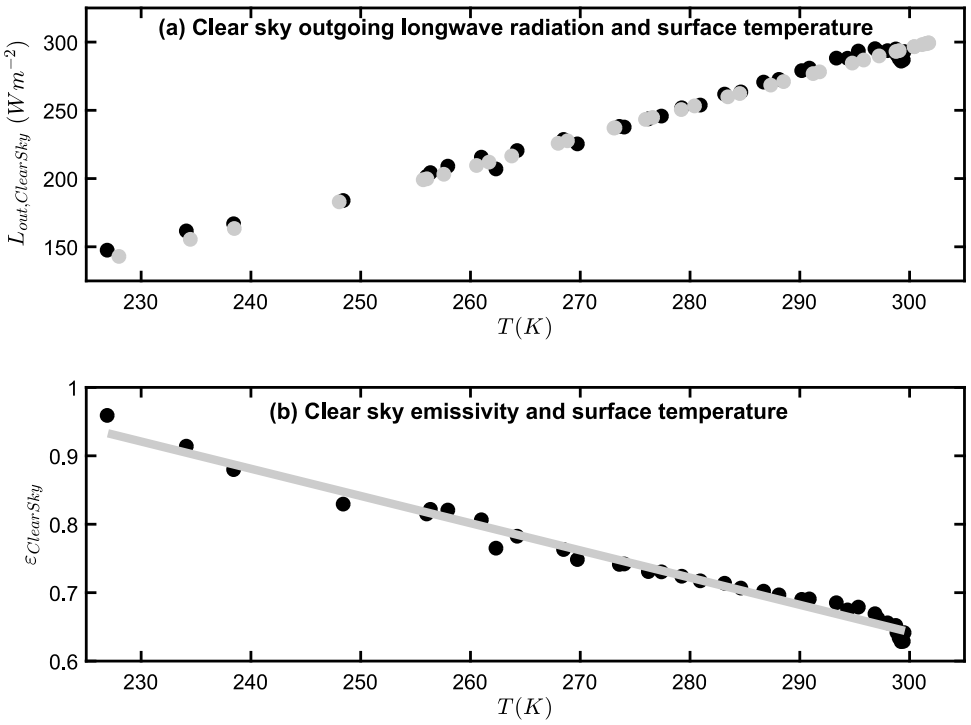

Fig. 3. Variation in annual- and zonal-mean clear-sky outgoing longwave radiation (a) and emissivity (b) with surface temperature. Observations (black dots) are calculated from CERES climatological satellite data for clear sky conditions [15], the CRUTEM absolute temperature reconstruction [14] and, for panel (b), calculations of daily average solar irradiance with latitude. Grey indicates (a) the initial spin up solution of the EBM (grey dots) and (b) a linear fitted approximation applied to the EBMs (grey line).

This expression, (11), is first used with climatological observations of cloud amount [16], averaged here to form the annual- and zonal-mean $f_{CA}(\phi)$ (Fig. 2e), to evaluate the annual- and zonal-mean emissivity of cloudy sky at latitude ϕ, $\varepsilon_{CloudySky}(\phi)$ (Fig. 2c, blue). Note that interpreting $\varepsilon_{CloudySky}(\phi)$ from (11) encapsulates the impact of clouds on emissivity during both fully clouded and partially clouded states, $0 < f_{CA}(\phi) \leq 1$.

A standard approach in conceptual EBMs is to vary outgoing longwave radiation as a linear function of surface temperature, $L_{out}(\phi) = AT_S(\phi) + B$ (e.g. [7–9,11,12]); a relationship supported by observational and theoretical arguments ([18]; see Fig. 3a, black) indicating a sensitivity in clear sky conditions of $\delta L_{out,ClearSky}/\delta T \approx 2$ $\mathrm{Wm^{-2}K^{-1}}$. Here, we seek an alternative approximation that uses surface temperature to calculate clear sky emissivity, instead of outgoing longwave radiation, so that Eq. (11) can then be utilised to explicitly calculate the impact of clouds.

Using Eq. (10), climatological reconstructions of $L_{out}(\phi)$ under all-sky and clear-sky conditions (Fig. 2a, black and orange) and climatological reconstruction of annual- and zonal-mean $T_S^4(\phi)$ (Fig. 2a, red), the emissivity with latitude is found under all-sky and clear-sky conditions, $\varepsilon_{AllSky}(\phi)$ and $\varepsilon_{ClearSky}(\phi)$ respectively (Fig. 2c). $\varepsilon_{ClearSky}(\phi)$ is found to be well approximated by a linear relationship to surface temperature (Fig. 3),

$$\varepsilon_{ClearSky}(\phi) = AT_S(\phi) + B \tag{12}$$

The conceptual EBM applies this linear relationship to calculate $\varepsilon_{ClearSky}(\phi)$ using $A = -3.9782 \times 10^{-3}$ $\mathrm{K^{-1}}$ and $B = 1.8359$ (with a maximum allowed value of $\varepsilon_{ClearSky} = 0.96$ and a minimum value of 0.40), and then also calculates the impact of cloudiness to result in all-sky emissivity. Note that applying (12) to the EBM here does produce a near-linear simulated relationship between outgoing longwave radiation and surface temperature for clear sky conditions (Fig. 3a, grey), with a gradient (2.16 $\mathrm{Wm^{-2}K^{-1}}$) consistent with observations (Fig. 3a, black) and previous analyses (e.g. 2.22 $\mathrm{Wm^{-2}K^{-1}}$ in [18]). Therefore, approximation (12) is consistent with previous EBMs adopting a linear relationship between outgoing longwave and surface temperature, with the benefit that the impact of clouds can be addressed via emissivity.

By comparing the clear-sky emissivity to the cloudy-sky emissivity (Fig. 2c), now consider how clouds affect the annual- and zonal-mean emissivity with latitude (Fig. 2c, blue and orange). A cloudy sky, where local cloud amount $f_{CA}(\phi) = 1$, acts to decrease the emissivity relative to clear-sky conditions, but by an amount that varies with latitude (Fig. 2c, varying distance between blue and orange lines). However, if we consider $1 - \varepsilon$ for the emitted longwave, then we can express the fraction by which cloudy skies decrease emissivity relative to clear skies with latitude, $c_\varepsilon(\phi)$, as,

$$c_\varepsilon(\phi) = \frac{1 - \varepsilon_{CloudySky}(\phi)}{1 - \varepsilon_{ClearSky}(\phi)} \tag{13}$$

Formally, $c_\varepsilon(\phi)$ is the annual mean fractional increase in 'one minus the emissivity of emitted surface longwave by the atmosphere per unit cloud amount' due to the presence of cloud at latitude ϕ. The resulting values of $c_\varepsilon(\phi)$, (13), in the real climate system are near-uniform with latitude (Fig. 2 g): the distribution of values of c_ε at 5° latitude intervals (Fig. 2e) has mean and standard deviation $c_\varepsilon(\phi) = 1.38 \pm 0.10$ (where 1.38 is the area-weighted mean and 0.10 is the standard deviation), with the small variation with latitude illustrating the consistent effect of clouds on longwave atmospheric absorptivity per unit cloud amount for climate states ranging from polar to tropical.

This near-uniform value of c_ε with latitude reveals information about the nature of the impact of clouds on emissivity of emitted longwave radiation (Fig. 2 g): clouds act to increase 1 minus the emissivity of a clear-sky atmosphere by a set fraction per unit cloud amount across a range of conditions, from tropical (clear sky emissivity $\varepsilon_{ClearSky}(\phi) \sim 0.6$, surface temperature $T_s \sim$

300 K) to polar (clear sky emissivity $\varepsilon_{ClearSky}(\phi) \sim 0.9$, surface temperature $T_s \sim 230$ K). At all latitudes the all-sky value of $1-\varepsilon_{AllSky}$, is increased by 0.38 ± 0.10 per unit cloud amount relative to the clear sky $1-\varepsilon_{ClearSky}$,

$$1-\varepsilon_{AllSky}(\phi) = \left[1-\varepsilon_{ClearSky}(\phi)\right]\left[1+(c_\varepsilon(\phi)-1)f_{CA}(\phi)\right] \quad (14)$$

The conceptual EBM uses a uniform value of $c_\varepsilon = 1.38$, and the imposed cloud amount with latitude, $f_{CA}(\phi)$ [16] (Fig. 2e), to calculate all-sky emissivity $\varepsilon_{AllSky}(\phi)$, from clear-sky emissivity $\varepsilon_{ClearSky}(\phi)$ and cloud amount.

2.3. Shortwave radiation and albedo

The total climatological annual- and zonal-mean outgoing shortwave radiation at latitude ϕ and under sky-condition i, $S_{out,i}(\phi)$ in Wm^{-2}, is given by the annual mean incoming solar radiation at ϕ, $R_{in}(\phi)$, multiplied by the albedo, $\alpha_i(\phi)$,

$$S_{out,i}(\phi) = R_{in}(\phi)\,\alpha_i(\phi) \quad (15)$$

The climatological annual- and zonal-mean albedo at latitude ϕ and under sky-condition i, $\alpha_i(\phi)$, is then formally defined as,

$$\alpha_i(\phi) = \int_t^{t+n\Delta t} \frac{S_{out,i}(\phi,t')}{R_{in}(\phi,t')}dt' \Big/ \int_t^{t+n\Delta t} dt' \quad (16)$$

Here, $R_{in}(\phi,t')$ is calculated from daily-mean values using the expressions and coefficients found in Hartmann [19]. From Eq. (16) and observational climatological reconstructions of $S_{out,AllSky}(\phi)$ and $S_{out,ClearSky}(\phi)$ (Fig. 2b), the annual- and zonal-mean albedo with latitude are estimated for clear sky and all-sky conditions, $\alpha_{ClearSky}(\phi)$ and $\alpha_{AllSky}(\phi)$ (Fig. 2d).

The conceptual EBM assumes all-sky albedo to be linearly composed of cloudy-sky albedo, $\alpha_{CloudySky}(\phi)$, multiplied by the fraction of incident solar radiation incident on clouds, $f_{CI}(\phi)$, and the clear-sky albedo, $\alpha_{ClearSky}(\phi)$, multiplied by the fraction of solar irradiance not incident on clouds, $[1-f_{CI}(\phi)]$, via,

$$\alpha_{AllSky}(\phi) = [1-f_{CI}(\phi)]\,\alpha_{ClearSky}(\phi) + f_{CI}(\phi)\,\alpha_{CloudySky}(\phi) \quad (17)$$

The annual- and zonal-mean fraction of solar irradiance incident on clouds, $f_{CI}(\phi)$, is subtly different from the fraction of cloud amount, $f_{CA}(\phi)$ (Fig. 2f, compare black to grey lines), because climatological mean cloud amount varies seasonally (e.g. [16]) and so too does incident solar irradiance, $R_{in}(\phi)$. Here, $f_{CI}(\phi)$ (Fig. 2f, black line) is calculated from monthly-mean values of the product of $f_{CA}(\phi,m)$ and $S_{in}(\phi,m)$, and then taking the annual time-average,

$$f_{CI}(\phi) = \frac{\sum f_{CA}(\phi,m)\,R_{in}(\phi,m)\,\Delta t_m}{\sum R_{in}(\phi,m)\,\Delta t_m} \quad (18)$$

where $f_{CA}(\phi,m)$ and $R_{in}(\phi,m)$ represent monthly mean values during month m, Δt_m is the mean duration of a month (such that all months are assumed to contribute equally to the annual mean), and the summation occurs over all 12 months.

2.3.1. Estimating the albedo of clouds

The conceptual EBM needs to calculate the albedo of cloudy-sky and all-sky conditions from terms representing the cloudiness, $f_{CI}(\phi)$, the albedo of cloud itself, $\alpha_{Cloud}(\phi)$, and the albedo of clear-skies, $\alpha_{ClearSky}(\phi)$. First, we consider how the albedo of cloud varies with latitude for the real climate system, and then this is used to inform a function form for the conceptual EBM. To perform this separation of $\alpha_{Cloud}(\phi)$ and $\alpha_{ClearSky}(\phi)$, we assume that clouds themselves are not a significant source of atmospheric absorption of solar shortwave radiation. Out of $\sim$340 Wm^{-2} of incoming solar radiation, approximately 80 Wm^{-2} is absorbed in the atmosphere [20]. We assume the majority of this shortwave atmospheric absorption is not due to the presence of clouds, but other agents such as aerosols, ozone and/or water vapour. This assumption allows us to write the outgoing solar radiation for a cloudy sky, $S_{out,CloudySky}(\phi) = R_{in}(\phi)\,\alpha_{CloudySky}(\phi)$, in terms of:

(i) the radiation directly reflected by the cloud, $R_{in}(\phi)\,\alpha_{Cloud}(\phi)$; and

(ii) the radiation that passes through the cloud on the way down, $R_{in}(\phi)\,[1-\alpha_{Cloud}(\phi)]$, is reflected off the surface (reducing by factor $\alpha_{ClearSky}(\phi)$), and then passed through the cloud again on the way up (reducing by further factor $1-\alpha_{Cloud}(\phi)$), resulting in additional outgoing radiation above the cloud of $R_{in}(\phi)\,\alpha_{ClearSky}(\phi)\,[1-\alpha_{Cloud}(\phi)]^2$.

Adding the outgoing radiation from direct cloud reflection, $R_{in}(\phi)\,\alpha_{Cloud}(\phi)$, to the outgoing radiation reflection from the surface having passed through the cloud in the way down and up, $R_{in}(\phi)\,\alpha_{ClearSky}(\phi)\,[1-\alpha_{Cloud}(\phi)]^2$, gives total outgoing reflected shortwave above a cloudy sky,

$$\begin{aligned} S_{out,CloudySky}(\phi) &= R_{in}(\phi)\,\alpha_{CloudySky}(\phi) \\ &= R_{in}(\phi)\,\alpha_{Cloud}(\phi) + R_{in}(\phi)\,\alpha_{ClearSky}(\phi)\,[1-\alpha_{Cloud}(\phi)]^2 \end{aligned} \quad (19)$$

where $\alpha_{Cloud}(\phi)$ is the albedo of cloud at latitude ϕ. The albedo for cloudy-sky conditions is then related to the albedo of cloud and the albedo of clear-sky conditions via,

$$\alpha_{CloudySky}(\phi) = \alpha_{Cloud}(\phi) + \alpha_{ClearSky}(\phi)\,[1-\alpha_{Cloud}(\phi)]^2 \quad (20)$$

This relation will be accurate, provided that the presence of the cloud is not significantly increasing local atmospheric absorption of shortwave radiation. Applying (20), along with the observation-derived estimates of $\alpha_{ClearSky}(\phi)$, $\alpha_{CloudySky}(\phi)$ and $f_{CI}(\phi)$ for recent climatology (Fig. 2h, black), we estimate that the albedo of clouds for the real climate system ranges from $\alpha_{Cloud} = 0.23$ at low latitudes up to 0.51 at high northern latitudes and 0.62 at high southern latitudes. The increasing α_{Cloud} at high latitudes is expected since the reflectance of solar radiation by clouds increases with the zenith angle of incident radiation (e.g. [21]). The global area-weighted mean of the observational implied estimate of cloud albedo, $\alpha_{Cloud}(\phi)$ (Fig. 2h, black), is $\overline{\alpha_{Cloud}}(\phi) = 0.32$, using Eq. (20).

This α_{Cloud} reconstruction presented here (Fig. 2h, black) represents a model interpreted, Eqs. ((17), (18), (20)), estimate of cloud albedo with latitude from satellite-based observations of outgoing radiation [15] and cloud amount [16], and calculations of incident solar radiation.

2.3.2. Conceptual closure for albedo varying with latitude, temperature and cloudiness

The conceptual EBM must now assume a function form describing how surface clear-sky albedo alters with latitude and temperature, and then how cloudiness affects all-sky albedo. First, we define $\overline{\alpha}_j$ as the mean planetary albedo for some surface type j. Many previous Energy Balance Models have used a 2nd order Legendre polynomial in $\sin\phi$ as the functional form to describe the change in albedo (or 1 – albedo, which is termed the coalbedo) over latitude for a uniform surface, or to approximate the entire Planetary surface with varying surface types (e.g. [9]). Legendre polynomials are particularly useful for generating straightforward solutions to EBMs using polynomial expansion. While this approach to generating solutions is not applied here, the Legendre polynomial form for albedo with latitude is retained to facilitate ease of comparison with previous studies. Some EBMs combine Legendre polynomials for some surface types with uniform albedo (or other functional forms) over latitude for other surface types (e.g. [8,22]), or have a single Legendre polynomial for the entire Earth surface including clouds (e.g. [8,9,12]).

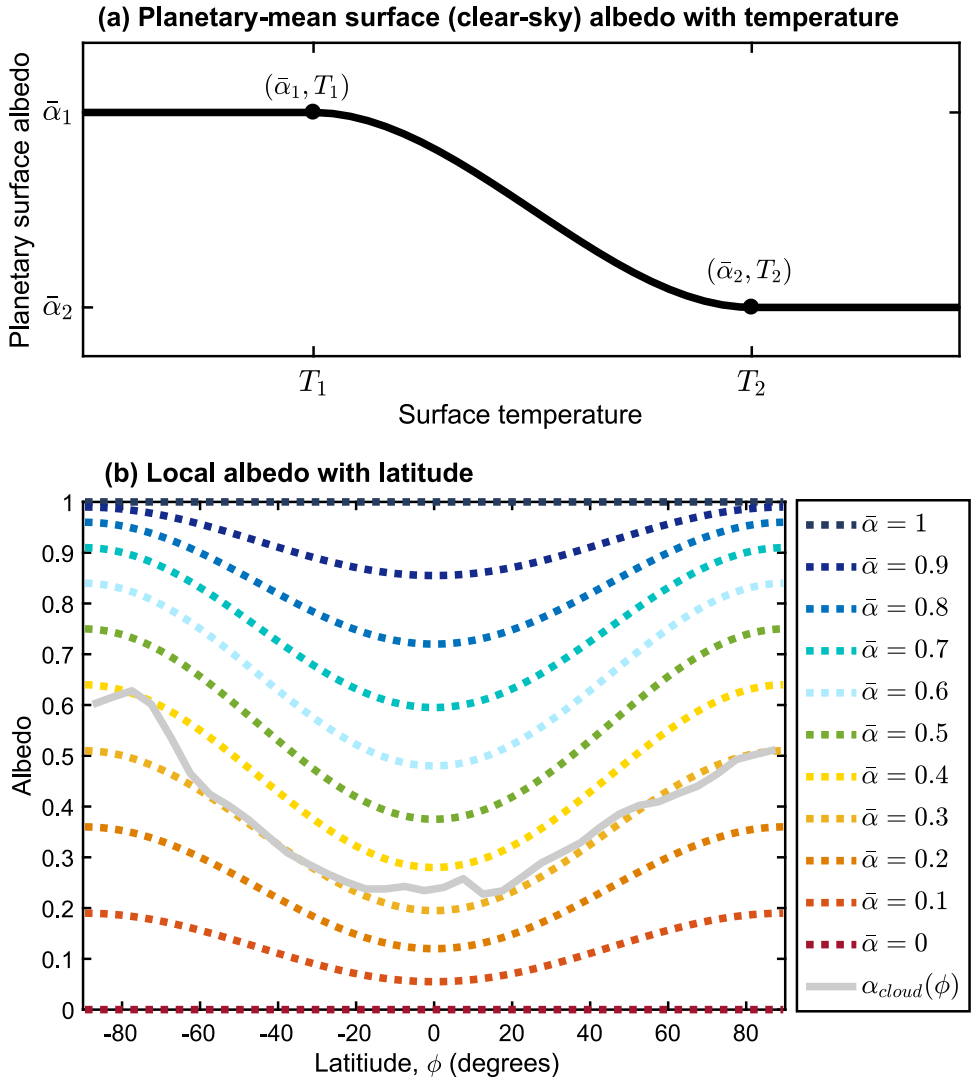

Fig. 4. Functional forms adopted for variation in albedo with temperature and latitude. (a) The global mean surface (clear-sky) global-mean albedo, $\overline{\alpha}$, when keeping the entire Earth's surface at some uniform temperature. (b) Functional form adopted for annual- and zonal-mean albedo with latitude for surfaces with different planetary albedo, ranging from 0 to 1 (dotted lines), and an estimate of cloud albedo interpreted from observations (grey solid line).

These approaches require a decision for each surface type as to whether to make the albedo latitudinally varying, via a Legendre polynomial, or constant with latitude. If latitudinally varying is chosen, then two coefficients must be specified: the first coefficient describing the mean planetary albedo for that surface-type, and the second coefficient describing how much the Planetary albedo changes with latitude. The EBM of Graves et al. [23] uses data to constrain a total of 36 coefficients (3 coefficients for each month of the year) applied to first and second order Legendre polynomials to calculate albedo with latitude and season, plus an additional coefficient to calculate the discontinuous albedo offset for when snow or ice is present. The EBM of Bitz and Roe [22] adopts an approach requiring specifying two coefficients for cryosphere-free albedo with latitude, a further coefficient for albedo of snow-covered land and a further two coefficients for albedo of sea-ice.

Here, we seek to reduce the number of choices and degrees of freedom by simply stating a single coefficient value for any given surface type that changes with surface temperature: $\overline{\alpha}(T_S)$ being the global mean clear sky surface albedo for a planet where the entire planetary temperature is fixed at T_S. $\overline{\alpha}(T_S)$ adopts a cubic form in T_S for $T_1 \leq T_S \leq T_2$ with turning points at $(T_2, \overline{\alpha}_2)$ and $(T_1, \overline{\alpha}_1)$. The values of $\overline{\alpha}(T_S)$ are held constant at the turning point values for all temperatures outside the range: $\overline{\alpha} = \overline{\alpha}_1$ for $T_S < T_1$, and $\overline{\alpha} = \overline{\alpha}_2$ for $T_S > T_2$ (Fig. 4a). T_2 is interpreted as the zonal- and annual-mean temperature above which there is no cryosphere and below which seasonal snow and ice on the ground begins to affect annual mean clear-sky albedo, and T_1 as the temperature below which the cryosphere entirely dominates the clear-sky albedo across all seasons.

The local clear-sky albedo at latitude ϕ and surface temperature T_S is then calculated within the EBM using the functional form,

$$\alpha(\phi, T_S) = \overline{\alpha}(T_S)\left[1 + [1 - \overline{\alpha}(T_S)]\left[\frac{1}{2}\left[3\sin^2\phi - 1\right]\right]\right] \tag{21}$$

where $0 \leq \overline{\alpha}(T_S) \leq 1$ for all T_S. The properties that make this closure (Eq. (21)) an attractive formulation include:

(1) If a surface-type is perfectly absorbing then it will remain perfectly absorbing for any latitude (Fig. 4b: when $\overline{\alpha} = 0, \alpha(\phi) = 0$ for all ϕ), and if a surface-type is perfectly reflecting then it will

Table 1
Tuneable parameter values used in the conceptual Energy Balance Models.

Conceptual EBM tuneable parameters	Value used
T_1: the temperature below which the Earth's surface albedo is dominated by the cryosphere	243.15 K
T_2: the temperature above which the Earth's surface albedo is unaffected by the cryosphere	268.15 K
$\overline{\alpha}_1$: the clear-sky planetary albedo of the Earth surface when albedo is dominated by the cryosphere	0.45
$\overline{\alpha}_2$: the clear-sky planetary albedo of the Earth's surface when unaffected by the cryosphere	0.17
$\overline{\alpha}_{Cloud}$: the planetary albedo of cloud, with cloud amount = 1 (assuming the surface below cloud level is perfectly absorbing)	0.32
H_{rel}: the relative humidity of the atmosphere[a]	0.70

[a]Only applied in the EBM variants with a moist atmosphere.

remain perfectly reflecting at any latitude (Fig. 4b: when $\overline{\alpha} = 1$, $\alpha(\phi) = 1$ for all ϕ);

(2) The local albedo will never be below 0 or above 1 at any latitude ϕ and for any value of $\overline{\alpha}$: $0 \leq \alpha(\phi, T_S) \leq 1$ for all ϕ and T_S when $0 \leq \overline{\alpha}(T_S) \leq 1$ for all T_S (Fig. 4b);

(3) The clear-sky albedo, $\alpha(\phi, T_S)$, is continuous and differentiable in both T and ϕ at all latitudes and all temperatures (Fig. 4a, b). While analytical solutions are not attempted here, this quality makes this approach (Eq. (21)) suitable for future analytical exploration;

(4) Surface albedo at any latitude and temperature is expressed with just 4 numerical parameters: $T_1, T_2, \overline{\alpha}_1, \overline{\alpha}_2$;

(5) The functional form accounts for differences in surface area with latitude such that the leading coefficient, $\overline{\alpha}(T_S)$, is always the area-weighted global mean clear-sky albedo.

The estimate presented here of cloud albedo in the real climate system with latitude is in good agreement with the functional form adopted for albedo with latitude for a given surface (Eq. (21), with $\overline{\alpha_{Cloud}}$ used in place of $\overline{\alpha}(T_S)$: Fig. 2h and Fig. 4b, compare solid to dashed lines), where area-weighted global mean cloud albedo is found to be $\overline{\alpha_{Cloud}} \approx 0.32$;

$$\alpha_{Cloud}(\phi) = \overline{\alpha_{Cloud}}\left[1 + [1 - \overline{\alpha_{Cloud}}]\left[\frac{1}{2}\left[3\sin^2\phi - 1\right]\right]\right] \tag{22}$$

Note that this estimate of cloud albedo can be interpreted as the albedo of a cloudy sky in the limit where all solar radiation passing through the cloud were perfectly absorbed below the cloud. The conceptual EBM calculates all-sky albedo as a function of temperature, T_S, latitude, ϕ, and cloud-incident solar radiation fraction, f_{CI}, using Eqs. (17), and ((20)–(22)) with values of $T_1, T_2, \overline{\alpha}_1, \overline{\alpha}_2$ and $\overline{\alpha_{Cloud}}$ given in Table 1.

2.4. Horizontal energy budget

The conceptual EBM used here adopts a diffusive model for horizontal heat transport, in common with many other EBMs (e.g. [8,9,11,12]). Here, we use the horizontal gradient in dry-bulb temperature, T_S, to diffuse heat horizontally via some effective diffusivity, $\kappa_{eff}(\phi)$ in W K^{-1} m^{-1},

$$f(\phi) = -\kappa_{eff}(\phi)\frac{\partial T_S}{\partial y}(\phi) \tag{23}$$

where $f(\phi)$ is the northward heat transport across the line of latitude ϕ per unit length of the line of latitude in W m^{-1}, and y is northward displacement in m. An observational implied value of $f(\phi)$ is acquired from calculations of the incident solar radiation with latitude and observational reconstructions of outgoing TOA energy (Fig. 5a, black), using an integral relation for total northward energy flux across a line of latitude [24],

$$F_{north}(\phi) = 2\pi r_{Earth}^2 \int_{\phi'=-\frac{\pi}{2}}^{\phi} (R_{in} - R_{out}) \cos\phi' d\phi' \tag{24}$$

where $F_{north}(\phi)$ in W is the total planetary heat northward flux across the line of latitude at ϕ (Fig. 5d, black) such that $f(\phi) = F_{north}(\phi)/(2\pi r_{Earth}\cos\phi)$; and the global mean area-weighted value of R_{in} is tuned so that it matches the corresponding observed value of R_{out}. This observation-implied value for $f(\phi)$ is combined with the observational reconstruction of $T_S(\phi)$, (Fig. 6c), to back-calculate an estimate for the effective diffusivity $\kappa_{eff}(\phi)$ for the real climate system (Fig. 5a, black dots). This effective diffusivity is applied to the conceptual EBM for preindustrial conditions. Note that at low latitudes the effective diffusivity cannot be calculated from observations, since heat is being transported up the dry-bulb temperature gradient. In these regions, the EBM diffusivity is prescribed using the value implied from observations closest to the equator (Fig. 5a, grey line and black dots). The effective diffusivity κ_{eff} varies over latitude for many reasons that are beyond the scope of this paper and are not solved for inside the conceptual EBM. Note that the latitudinal variation in κ_{eff} applied here (Fig. 5a, black dots) is empirically determined. Previous studies have adopted non-uniform diffusivity via alternative methods, for example via linear or non-linear functional forms (e.g. [25,26]), while the original Budyko [7] EBM applied a linear relaxation to the global mean temperature.

2.5. Simulating preindustrial steady state in the conceptual EBM

The EBM is numerically configured with $i = 36$ discrete horizontal locations (Fig. 7) giving a resolution of 5° latitude (spaced from −87.5° to +87.5°). Fields for $\kappa_{eff}(\phi)$, $f_{CA}(\phi)$, $f_{CI}(\phi)$ and $R_{in}(\phi)$ are imposed and the initial temperature is set to $T_S(\phi) = 273.15$ K at all latitudes. A uniform value of heat capacity per unit surface area is defined ($c = 4.2 \times 10^8$ J K^{-1} m^{-2}, corresponding to a 150 m deep surface ocean mixed layer covering 70% of the Earth's surface) and the model is run to an initial steady state, broadly intended to simulate the preindustrial climate. At steady state, the net energy increase from vertical radiation balance and horizontal energy flux is 0 at all latitudes such that Eq. (6) becomes,

$$0 = R_{in}(\phi) - R_{out}(\phi) - \frac{\partial f}{\partial y}(\phi) \tag{25}$$

From the observation-implied fields for horizontal diffusivity, $\kappa_{eff}(\phi)$ (Fig. 5a), and cloudiness, $f_{CA}(\phi)$, $f_{CI}(\phi)$ (Fig. 2e,f), and calculated incident radiation, $R_{in}(\phi)$, the EBM applies equations ((5),(6), (8)–(24)) to simulate annual- and zonal-mean vertical energy balance, heat transport and surface temperatures (Fig. 6, grey).

The simulated variables in the conceptual EBM compare well to the real climate system in terms of the variation with latitude of the simulated variables: TOA energy imbalance (Fig. 6a), TOA outgoing longwave and shortwave energy fluxes (Fig. 6b), steady state temperatures (Fig. 6c), poleward energy transport (Fig. 6d), all sky albedo (Fig. 6e), and all sky emissivity (Fig. 6f). There are clearly many functional form of equations one could specify that would not simulate values of $T_S(\phi)$, $L_{out}(\phi)$, $S_{out}(\phi)$, $F_{North}(\phi)$, $\alpha_{AllSky}(\phi)$ and $\varepsilon_{AllSky}(\phi)$ that approximate real-world values, even when forced with accurate values for $\kappa_{eff}(\phi)$, $f_{CA}(\phi)$, $f_{CI}(\phi)$ and $R_{in}(\phi)$. Therefore, the similarity of simulated quantities to observations (Fig. 6) provides confidence in the EBM approach (Fig. 7) and functional form of the equations presented here, Eqs. ((5), (6), (8)–(24)). The near-linear relationship between outgoing

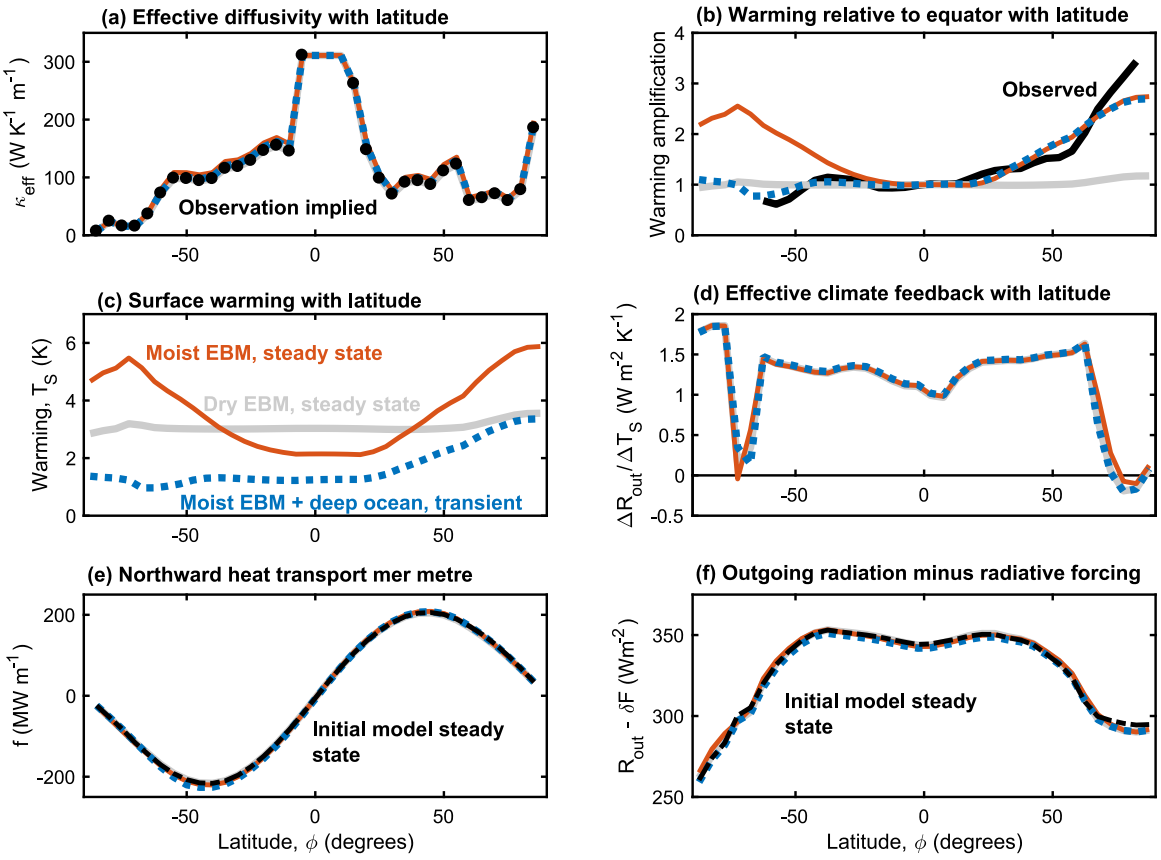

Fig. 5. (a) Effective horizontal diffusivity with latitude, (b) Surface warming with latitude, (c) Amplification in surface warming with latitude, relative to the equator, (d) Climate feedback with latitude, calculated via $\Delta R_{out}/\Delta T$ where Δ indicates the change from the initial model spin up to the final model state. (e) Simulated northward horizontal heat transport per East–West metre with latitude, $f\,(\phi)$. (f) Simulated outgoing radiation minus imposed radiative forcing with latitude. All panels show the dry atmosphere EBM simulation (grey), moist atmosphere EBM simulation (red) and moist atmosphere EBM plus deep ocean, transient after 20 years (blue dotted line). Panels (a) and (b) show observations (black). Panels (e) and (f) show the initial EBM spin up (black dot-dashed lines).

longwave radiation and surface temperature in the preindustrial steady state simulations (Fig. 3a, grey) are both a good match to observations (Fig. 3a, black; [18]) and show that the conceptual EBM is consistent with previous EBMs that enforce a linear parameterisation (e.g. [7,8], [9,11], [12])

Section 3, 4 and 5 now test how alternative versions of the EBM (Fig. 7; Fig. 6, grey) respond to a perturbation in terms of surface warming with latitude. While the equations above are general, there must be further approximations in terms of how we calculate the applied fields, $\kappa_{eff}\,(\phi)$, $f_{CA}\,(\phi)$ and $f_{CI}\,(\phi)$, when the system is perturbed, given that we only have observational reconstructions for past values. First, all following sections consider a constant cloud approximation, and so the fields for $f_{CA}\,(\phi)$ and $f_{CI}\,(\phi)$ remain unchanged. There may be explanations for Arctic Amplification and reduced warming at Southern high latitudes that require latitudinally varying cloud responses to warming; these explanations will not be explored in this study. In the first EBM variant, Section 3 applies a constant effective diffusivity approximation, keeping $\kappa_{eff}\,(\phi)$ unchanged with future warming. Meanwhile, a second EBM variant is considered in Section 4, where $\kappa_{eff}\,(\phi)$ may alter due to thermodynamic responses in the EBM as surface temperatures warm with a moist atmosphere. Section 5 presents a third EBM variant that includes the deep ocean to explore how heat exchange between the surface climate layer and the deep ocean may affect surface warming with latitude.

3. Simulated warming response with a dry-atmosphere approximation

Here an idealised latitudinally-uniform radiative forcing, Eq. (8). of $\delta F\,(\phi) = 3.71\,\mathrm{Wm}^{-2}$ is imposed on the initial steady state EBM (Fig. 6, grey), and the model is run to a final steady state such that energy budget is re-balanced at all latitudes. This magnitude in idealised radiative forcing is chosen to represent an instantaneous doubling of atmospheric CO_2, although note that the radiative forcing from increased CO_2 is not truly uniform with latitude and there are other historical sources of radiative forcing (e.g. [5,27]). Any radiative forcing (e.g. reducing the outgoing radiation from an increase in greenhouse gas concentrations) must be eventually re-balanced by some combination of the change in outgoing radiation from the surface temperature response, $\delta\, R_{out,AllSky}\big|_{\delta T}\,(\phi)$, and the latitudinal change in net horizontal heat flux, $\delta\left[\frac{\partial f}{\partial y}\right](\phi)$, Eq. (8).

The first conceptual EBM is produced by perturbing the initial steady state with a radiative forcing while holding $\kappa_{eff}\,(\phi)$, $f_{CA}\,(\phi)$ and $f_{CI}\,(\phi)$ constant in time (Fig. 5a; Fig. 2e,f). The local heat flux supplied by horizontal heat transport per unit area at latitude ϕ, $\frac{\partial f}{\partial y}\,(\phi)$ in Wm^{-2}, is then given by the partial derivative of f, Eq. (22), with northward distance. With the effective diffusivity unaffected by local temperature in this EBM variant, then the horizontal heat flux simplifies to,

$$\frac{\partial f}{\partial y}\,(\phi) = -\kappa_{eff}\,(\phi)\,\frac{\partial^2 T}{\partial y^2}\,(\phi) \tag{26}$$

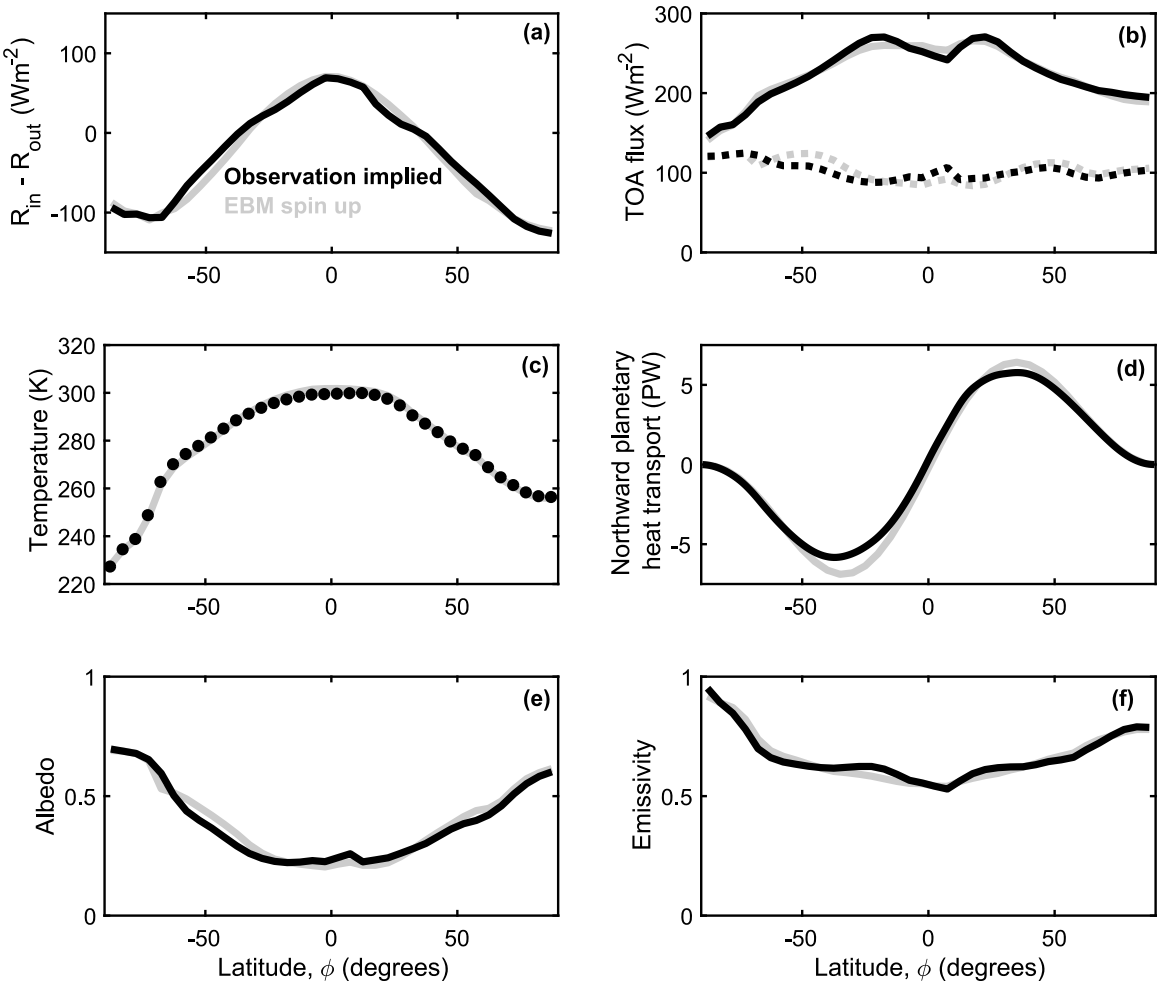

Fig. 6. Comparison of EBM initial spin up (grey lines) to observations (black lines) for annual- and zonal-mean quantities with latitude. (a) The net top-of-the-atmosphere (TOA) energy imbalance. (b) Outgoing TOA longwave (solid lines) and shortwave (dotted lines) radiation. (c) Surface temperature. (d) Total northward planetary heat transport, $F_{North}(\phi) = f(\phi)\, r_{Earth} \cos\phi$. (e) All-sky albedo. (f) All-sky emissivity. The observation-implied global mean $T = 287.1$ K (1961–1990), while the EBM initial spin up global mean $T = 288.1$ K (preindustrial spin up).

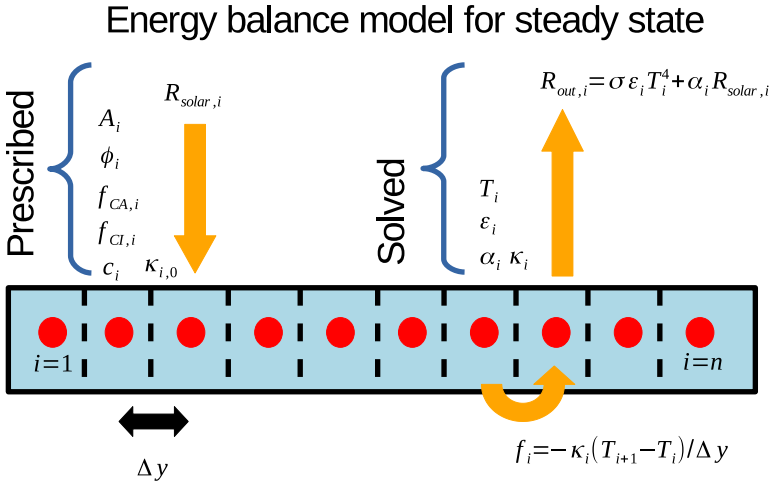

Fig. 7. Schematic of the conceptual Energy Balance Model used for finding the steady state latitudinal temperatures including a top-of-the-atmosphere radiation budget of incoming solar radiation and outgoing solar and longwave radiation, together with the effect of meridional heat transport.

This approximation, Eq. (26), is used here as implying a dry atmosphere, since with moisture then a significant component of the horizontal heat transport, f, will be due to latent heat and the fraction due to latent heat will vary with temperature causing $\kappa_{eff}(\phi)$ to also vary with temperature.

With $\kappa_{eff}(\phi)$ held constant in time (Fig. 5a, grey line and black dots), the global mean area-weighted surface temperature increases by 3.04 K relative to the initial steady state (Fig. 5c, grey line), in agreement with the latest best estimates for the warming following a doubling of atmospheric CO_2 for the real climate system of 3.0 K [1]. However, the pattern of warming in the conceptual EBM shows very little Polar Amplification in either hemisphere (Fig. 5b,c, grey lines), at odds with the Arctic Amplification observed in the real climate system (Fig. 5b, black line).

The effective climate feedback with latitude in this first EBM variant is calculated by dividing the change in outgoing radiation at TOA due to rising surface temperatures by the change in surface temperature, $\frac{\Delta R_{out,AllSky}}{\Delta T_S}(\phi)$, from the initial steady state to the final warmed steady state in the EBM. Radiative climate feedbacks do show significant variation from low latitudes to the poles (Fig. 5c, grey). The very low magnitude climate feedback regions at high latitudes in both hemispheres indicate where surface albedo is changing due to surface warming in the EBM.

A lower value for local climate feedback, $\frac{\Delta R_{out,AllSky}}{\Delta T}(\phi)$, could imply a large local temperature change is required to re-balance a radiative forcing. However, even though local climate feedback goes toward 0 near the poles the local temperature change does not see a great amplification in this EBM variant. At high latitudes, this implies that the change in divergence in horizontal heat transport is balancing the radiative forcing, rather than an increase in local outgoing radiation. Therefore, this first EBM variant demonstrates that even very large localised vertical radiative feedback at high latitudes (e.g. from surface albedo feedback: Fig. 5d, grey) is not enough to produce the significant observed Arctic Amplification (Fig. 5b,c, compare grey to black) if effective horizontal diffusivity (of heat via the dry-bulb temperature gradient) is held constant (Fig. 5a, black and grey).

Dry atmosphere EBMs rely on latitudinal differences in either radiative forcing or radiative feedbacks to achieve Arctic Amplification [9]. While some dry atmosphere EBMs with different parameterisations display larger Arctic Amplification than the empirically constrained model used here (e.g. [28]), moist static EBMs do display larger Arctic Amplification than similar dry atmosphere EBMs (e.g. [9,28]). The next section presents a second EBM variant, where effective diffusivity varies with local surface temperature due to atmospheric moisture.

4. Simulated warming response with a moist atmosphere approximation

In the EBM version considered above, horizontal effective diffusivity is unaffected by surface temperature change such that f in Eq. (23) is differentiated to give $\frac{\partial f}{\partial y}$ via Eq. (26). However, if the effective diffusivity is dependent on local surface temperature, then we must consider how the latitudinal change in diffusivity with temperature affects $\frac{\partial f}{\partial y}$, such that Eq. (23) is differentiated to give,

$$\frac{\partial f}{\partial y}(\phi) = -\frac{\partial}{\partial y}\left[\kappa_{eff}(\phi)\frac{\partial T_S}{\partial y}(\phi)\right] \tag{27}$$

To model the diffusivity-temperature dependence, $\kappa_{eff} = \kappa_{eff}(\phi, T)$, in the second EBM variant presented in this section, we take inspiration from recent moist-static EBMs (e.g. [9]). Merlis and Henry [9] found that an EBM that diffused moist static energy (including both dry static energy and latent energy storage) does reproduce a larger magnitude of Polar Amplification, consistent with observations and more complex models [9]. Thus, we consider here how $\kappa_{eff}(\phi)$ changes according to the change in the ratio of dry static energy transport to latent energy transport as a parcel of air is warmed or cooled.

4.1. Effective horizontal diffusivity and temperature in the moist atmosphere EBM

Here, the thermodynamic processes that may alter the effective horizontal diffusivity are explored. First, consider the total horizontal energy transport per unit latitudinal length, $f(\phi)$, in terms of contributions from dry-static air, latent heat within air and heat transport within the ocean,

$$\begin{aligned} f(\phi) &= f_{dry}(\phi) + f_{latent}(\phi) + f_{ocean}(\phi) \\ &= -\left[\kappa_{dry}(\phi) + \kappa_{latent}(\phi) + \kappa_{ocean}(\phi)\right]\frac{\partial T_S}{\partial y}(\phi) \end{aligned} \tag{28}$$

The overall effective diffusivity may therefore be approximated in terms of a dry static diffusivity, and latent heat diffusivity and an ocean diffusivity, which simplifies in regions where the atmosphere is the dominant medium through which poleward heat transport occurs,

$$\kappa_{eff}(\phi) = \kappa_{dry}(\phi) + \kappa_{latent}(\phi) + \kappa_{ocean}(\phi) \approx \kappa_{dry}(\phi) + \kappa_{latent}(\phi) \tag{29}$$

In areas where ocean heat transport is low (from mid to high latitudes), we may write the effective diffusivity via,

$$\kappa_{eff}(\phi, T_S) \approx \kappa_{dry}(\phi)\left[1 + r_{latent:dry}(T_S)\right] \tag{30}$$

where $r_{latent:dry}(T_S) = \frac{\kappa_{latent}}{\kappa_{dry}}$ is the ratio of latent to dry heat transport. The effective diffusivity at ϕ and T_S is then related to the effective diffusivity at ϕ and T_0 via,

$$\kappa_{eff}(\phi, T_S) \approx \kappa_{eff}(\phi, T_0)\left[\frac{1 + r_{latent:dry}(T_S)}{1 + r_{latent:dry}(T_0)}\right] \tag{31}$$

where we may set T_0 to be the preindustrial temperature at latitude ϕ. This choice allows us to alter the effective diffusivity from the preindustrial effective diffusivity in the conceptual EBM with latitude as the temperatures change from their initial preindustrial steady state values.

The value of $r_{latent:dry}(T_S)$ is calculated by considering the ratio of dry and latent energy change for a parcel of air when it changes temperature, T_S, but has relative humidity H_{rel} held constant,

$$r_{latent:dry}(T_S) = \frac{H_{rel}L}{1000 \times c_p} \times \frac{\partial q^*}{\partial T_S} \tag{32}$$

where L is the latent heat of vaporisation (with $L = 2.6 \times 10^6$ J kg^{-1} used in the EBM), c_p ($= 3910$ J K^{-1} kg^{-1}) is the specific heat capacity of dry air, and q^* is the specific humidity at saturation. The specific humidity at saturation, q^*, is approximated as a function of T_S via the Clausius-Clapeyron relation,

$$q^*(T_S) \approx k \times \exp\left\{\frac{L}{R_v}\left[\frac{1}{273} - \frac{1}{T_S}\right]\right\} \tag{33}$$

where k is some constant and R_v is the gas constant for water vapour of 461 J K^{-1} kg^{-1}. The value for k used in the conceptual EBM ($k = 3.111$) is adapted from Hartmann [19] (see Appendix B therein). Differentiating the specific humidity at saturation with temperature results in,

$$\frac{\partial q^*}{\partial T_S} \approx \frac{kL}{R_v T^2}\exp\left[\frac{L}{R_v}\left\{\frac{1}{273} - \frac{1}{T_S}\right\}\right] \tag{34}$$

By inspecting Eqs. (32) and (34) we see that the ratio of latent to dry heat exchanged when a parcel of air changes temperature

at constant relative humidity increases approximately exponentially with temperature. Therefore, increasing surface temperatures, $T_S > T_0$, will increase the effective horizontal diffusivity, $\kappa_{eff}(\phi, T_S) > \kappa_{eff}(\phi, T_0)$. Such an increase in $\kappa_{eff}(\phi, T_S)$ with increased T_S may be expected to contribute to Polar Amplification of warming via increased efficiency of poleward heat transport (i.e. the same poleward heat transport could be achieved via a reduced equator to pole dry-bulb temperature gradient).

4.2. The moist EBM warming response at steady state

The second EBM variant, used in this section, considers effective diffusivity as a function of both latitude and temperature, $\kappa_{eff} = \kappa_{eff}(\phi, T_S)$, Eqs. ((27)–(34)). This second EBM uses the same initial steady state (Fig. 6, grey), which is again perturbed with a uniform radiative forcing of 3.71 Wm^{-2} while holding $f_{CA}(\phi)$ and $f_{CI}(\phi)$ constant in time. However, now the numerical integration of the model calculates $\kappa_{eff}(\phi, T_S)$ from the initial $\kappa_{eff}(\phi)$ field (Fig. 5a, black) and the change in local surface temperature relative to the initial simulated temperature (Eqs. (31)–(34)). Note that the EBM values of $\kappa_{eff}(\phi)$ are not varied from the initial steady state as the model is warmed at low latitudes where the original value of $\kappa_{eff}(\phi)$ is above 200 W K^{-1} m^{-1} (Fig. 5a, black and red). This is because when $\kappa_{eff}(\phi)$ is very large originally, the approximations within Eqs. ((28)–(34)) cannot be assumed. Firstly, at low latitudes heat may be transported due to changes in relative humidity between the humid tropics and the arid subtropics, and so H_{rel} cannot be assumed to be constant. Secondly, the ocean becomes more significant in poleward heat transport at low latitudes.

Once the second EBM reaches a final steady state the rise in global mean surface temperature in response to the imposed radiative forcing is 3.06 K, approximately the same as the first EBM and remaining in agreement with the recent best estimate of 3.0 K warming for a doubling of CO_2 for the real climate system [1]. The rise in effective diffusivity from the warming appears relatively modest, and is greatest at mid-latitudes (Fig. 5a, compare red to black and grey). However, the spatial pattern of warming in the second EBM shows much greater Polar Amplification than the first EBM in both hemispheres (Fig. 5b,c). The impact of the modest rise in effective diffusivity, from a rising fraction of latent heat transport to dry heat transport as temperatures warm, increases polar amplification of surface warming in agreement with the observed warming in the Arctic (Fig. 5b, compare red to black).

Therefore, the second EBM shows that high latitude radiative climate feedbacks (from surface albedo effect; Fig. 5d, red) when coupled with temperature-dependent effective horizontal diffusivity (from the Clausius-Clapeyron relation altering the relative latent heat to dry heat contribution; Fig. 5a, red) can act together to give Arctic Amplification of surface warming at a similar magnitude to observations of the recent anthropogenic warming (Fig. 5b, red and black).

However, the simulated warming shows significant amplification in both hemispheres, while the observed pattern shows reduced warming at southern high latitudes (Fig. 5b, red and black). One key difference is that the simulated warming response refers to the change between an initial and final steady state, whereas the current anthropogenic warming is in a transient state. The next section introduces the third EBM variant by coupling the EBM to a deep ocean heat reservoir, and simulates transient warming with latitude including transient heat exchange between the surface climate layer and the deep ocean.

5. Transient warming response with moist atmosphere EBM plus deep ocean

The third EBM variant considered here extends the moist-atmosphere variant (Section 4) by coupling the surface climate layer of the EBM to a deep ocean heat reservoir (Fig. 8). This extension is accomplished by adapting a commonly used global-mean ocean model with a surface mixed layer and deep ocean reservoirs that exchange heat.

5.1. Two-layer ocean, global-mean climate model

Inspiration is drawn from a classic 2-layer ocean, global-mean climate model, with an atmosphere plus surface ocean mixed layer heat reservoir attached to a deep ocean layer heat reservoir. A concise and useful mathematical description for this two-layer climate model is found in Gregory [13], with solutions for idealised forcing scenarios. The deep ocean is relatively very large and so has a large heat capacity, while the surface climate layer has a much smaller heat capacity. Revisiting equations that describe this simple two-layer climate system we have, for a uniform global mean surface climate layer,

$$c_s \frac{d\overline{T_s}}{dt} = \overline{R_{in}} - \overline{R_{out}} + \overline{h_s} = \overline{R_{in}} - \overline{R_{out}} + \overline{\gamma}\left[\Delta\overline{T_d} - \Delta\overline{T_s}\right] \tag{35}$$

where an overbar indicates a global spatial mean value; $\Delta\overline{T_d}$ and $\Delta\overline{T_s}$ are the changes in deep ocean temperature and surface climate temperature relative to the initial steady state respectively; $\overline{h_s} = \overline{\gamma}\left[\Delta\overline{T_d} - \Delta\overline{T_s}\right]$ is the heat transport from the sub-surface ocean upwards into the surface mixed layer of the ocean in Wm^{-2}; and γ is the efficiency of vertical heat transport between the surface and deep ocean in $Wm^{-2}K^{-1}$. Note the absence of a horizontal heat flux term in Eq. (35), since this classic approach only considers the global mean surface temperature. The equation for the rate of change of temperature of the deep ocean is then,

$$c_d \frac{d\overline{T_d}}{dt} = \overline{h_d} = -\overline{h_s} = \gamma\left[\Delta\overline{T_s} - \Delta\overline{T_d}\right] \tag{36}$$

In reality, the upwelling of water from the deep ocean into the surface, and downwelling from the surface into the deep, are both highly varying spatially (e.g. [19,29]). Therefore, the efficiency of heat exchange between the surface ocean and deep ocean, γ, must also be spatially varying and will vary spatially differently for upwelling than for downwelling since locations of ocean downwelling are different to the locations of ocean upwelling.

5.2. Extending the two-layer ocean, climate model to include latitudinal variations

The two-layer ocean global mean climate model (Eqs. (35)–(36)) is now used to extend the Energy Balance Model to include latitudinally-varying heat exchange between the surface climate and the deep ocean (Fig. 8).

If we continue to treat the deep ocean as a uniform heat reservoir, but consider the spatial variation in surface ocean temperatures, then we are interested in the spatial variation in the efficiency of heat exchange via upwelling of water from the deep ocean into the surface ocean. The third EBM presented in this section (Fig. 8) includes the heating of the surface ocean through exchange with the deep ocean at latitude ϕ, h_s in Wm^{-2}, based upon the product of the local efficiency of deep-to-surface ocean heat exchange, $\gamma(\phi)$ in $Wm^{-2}K^{-1}$, and the change in global mean deep ocean temperature minus the change in local surface temperature,

$$h_s(\phi) = \gamma(\phi)\left[\Delta\overline{T_d} - \Delta T_s(\phi)\right] \tag{37}$$

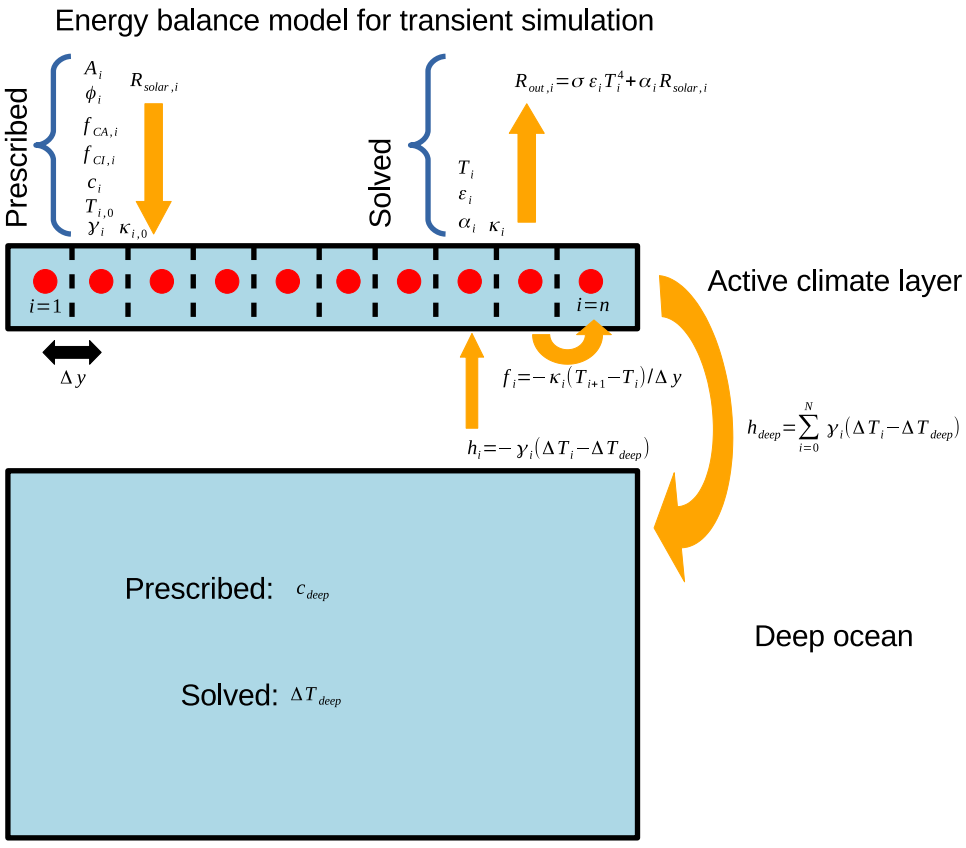

Fig. 8. Schematic of the conceptual Energy Balance Model used for evaluating the transient latitudinal warming, extending the previous Energy Balance Model (Fig. 7) by including ocean heat transfer from an active climate layer representing the atmosphere and surface ocean mixed layer to the deep ocean. Schematic has n = 10 latitudinal bands, whereas the numerical model used has n = 36 latitudinal bands.

where Δ indicates the change relative to the initial steady state condition (Fig. 6, grey). Note that $h_s(\phi)$ is the *change* in vertical heat flux through the base of the ocean surface mixed layer relative to the initial steady state in Wm^{-2}, and that this equation is not seeking to calculate the total value of ocean heat exchange at that location. At the initial steady state, all heat fluxes from one latitude band to another latitude are encapsulated within the tuned horizontal diffusivity values (κ_{eff}: Fig. 5a), whether they occur through the surface climate or via the deep ocean.

The Gregory [13] version of this 2-layer climate model uses $\gamma = 1.6\ \mathrm{W\,m^{-2}\,K^{-1}}$ as the uniform value for efficiency of heat exchange between the surface and deep ocean, constrained against a complex ocean model. Meanwhile, DeVries and Primeau [29] calculate that 62.5% of water currently in the deep ocean will first upwell into the surface ocean between 50° South and 70° South, due to the upwelling of a water mass known as circumpolar deep water. Therefore, in the moist EBM with deep ocean, we set $\gamma(\phi)$ such that the spatial mean $\gamma(\phi)$ is equal to 1.6 $\mathrm{W\,m^{-2}\,K^{-1}}$ and 62.5% of the global area-integrated total $\gamma(\phi)$ lies between 50° S and 70° S (Fig. 9a).

The vertical heat transport from the deep ocean into the surface ocean mixed layer must be equal and opposite to the heat transport from the surface ocean mixed layer into the deep ocean, but crucially this heat transport does not have to balance at all latitudes. Therefore, the EBM calculates the vertical heat transport into the deep ocean via,

$$\int h_d\,(\phi)\,dA = -\int h_s\,(\phi)\,dA \tag{38}$$

where dA is the area element with latitude ϕ. The next subsection considers how this global mean approach (Eqs.(35)–(38)) may be extended to the latitudinally varying EBM.

5.3. The moist atmosphere EBM plus vertical heat exchange with deep ocean

In reality, there are local heat exchanges between the surface ocean and deep ocean at steady state (e.g. [19]), which must globally sum to zero while the mean temperatures of both the surface and deep ocean remain constant in time. In the EBM, these steady state vertical heat exchanges are included within the observationally-derived values of horizontal effective diffusivity, $\kappa_{eff}\,(\phi)$ (Fig. 5a, black). First, consider how the annual- and zonal-mean energy balance at latitude ϕ, Eq. (6), is altered by an upwelling of heat across the deep ocean to surface ocean boundary. The total rate of heating of the surface climate at latitude ϕ becomes,

$$c\,(\phi)\,\frac{\partial T_s}{\partial t}\,(\phi) = R_{in}\,(\phi) - R_{out}\,(\phi) + \frac{\partial f}{\partial y}\,(\phi) + h_s(\phi) \tag{39}$$

while the equation describing the rate of heat content change in the deep ocean is,

$$c_{deep}\frac{dT_{deep}}{dt} = \frac{\int h_d\,(\phi)\,dA}{A_{ocean}} = -\frac{\int h_s\,(\phi)\,dA}{A_{ocean}} = -\frac{\int \gamma\,(\phi)\left[\Delta T_{deep} - \Delta T\,(\phi)\right]dA}{A_{ocean}} \tag{40}$$

In the active surface climate system (atmosphere plus surface ocean) we therefore have substituting Eqs. (27) and (37) into (39),

$$c\,(\phi)\,\frac{\partial T_s}{\partial t}\,(\phi) = R_{in}\,(\phi) - R_{out}\,(\phi) - \frac{\partial}{\partial y}\left[\kappa_{eff}\,(\phi, T)\,\frac{\partial T}{\partial y}(\phi)\right] + \gamma(\phi)\left[\Delta T_{deep} - \Delta T\,(\phi)\right] \tag{41}$$

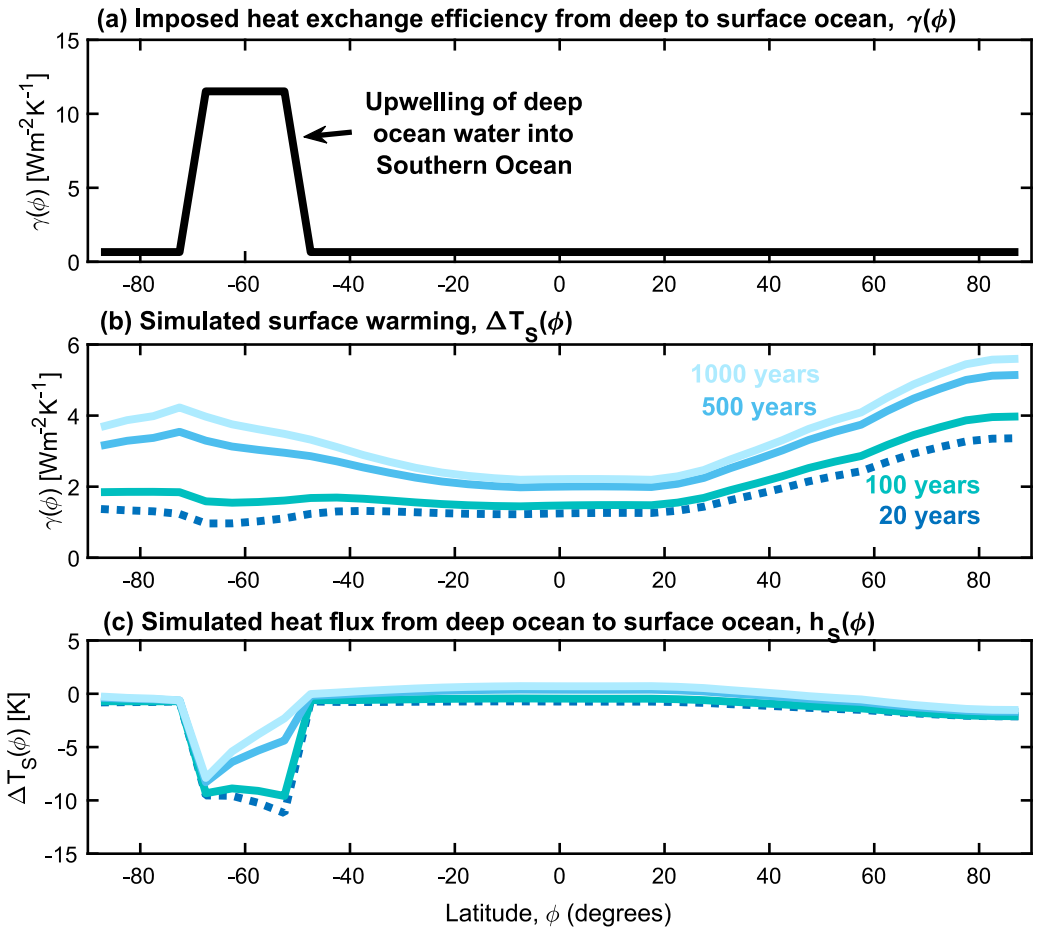

Fig. 9. Responses of the third EBM variant with moist atmosphere plus deep ocean heat exchange. (a) Imposed efficiency of heat exchange from deep to surface ocean with latitude. (b) Simulated warming 20, 100, 500 and 1000 years after a uniform 3.71 Wm^{-2} radiative forcing is imposed. (c) Simulated heat flux from the deep ocean to the surface ocean 20, 100, 500 and 1000 years after a uniform 3.71 Wm^{-2} radiative forcing is imposed.

Previous EBMs have been coupled to a representation of deep ocean heat exchange (e.g. [30–32]). Beer et al. [30,31] vary the exchange coefficient between the surface climate layer and deep ocean (equivalent to γ in this study) depending only on the presence of sea-ice and do not consider other latitudinal variation, for example due to the locations of upwelling (Fig. 9a). Hill et al. [32] adopt a different approach, forcing an EBM with a latitudinal field for the heat exchange (equivalent to h_s in this study) obtained from a complex climate model at various time slices. This is equivalent to specifying $h_s(\phi)$ in Eq. (39) without linking this to the EBM simulated surface to deep temperature contrast (Eqs. (37), (41)).

5.4. Warming responses in the EBM with moist atmosphere plus deep ocean heat exchange

As with the previous two EBM variants (Sections 3 and 4), the third EBM variant begins with the same initial steady state (Fig. 6, grey), and is then perturbed with an instantaneous uniform radiative forcing of 3.71 Wm^{-2}. Unlike EBM variants 1 and 2, this model is used to produce simulations of transient warming before the energy budget is fully restored to an equilibrium. EBM variant 3 is run for a set number of simulated years in time after the radiative forcing: 20, 100, 500 and 1000 simulated years (Fig. 9). After 20 years the global-mean surface warming reaches 1.5 K (Fig. 9b) and 49% of the initial radiative forcing has been balanced by an increase in outgoing radiation. After 100 years the warming reaches 1.8 K and 60% of the radiative forcing has been balanced, while after 500 years warming reaches 2.6 K and 86% has been balanced, and after 1000 years warming reaches 2.9 K and 96% of the radiative forcing has been balanced (Fig. 9b), indicating that the 1000-year simulation is approaching the final steady state in response to radiative forcing.

After both 20 and 100 years there is a significant hemispheric asymmetry in the simulated warming response (Fig. 9b), with strongly amplified warming in the Arctic and reduced warming in southern high latitudes, at the location of greatest upwelling efficiency of heat exchange from the deep ocean to the surface ocean (Fig. 9a,c). After 500 to 1000 years, the transient effect of reduced warming in the southern high latitudes decreases (Fig. 9b), as the deep ocean warms and the cooling impact of upwelling deep water into warmed surface water weakens (Fig. 9c).

The relative amplification of warming with latitude in the transient cases (20 or 100 years after imposed radiative forcing: Fig. 9b) is similar in magnitude in both hemispheres to the observed warming pattern over the last 100 years (Fig. 5b, compare blue dotted line to black line). Thus, this third conceptual EBM (Fig. 8) illustrates how both the magnitudes of Arctic amplification and reduced warming at ∼55° S (Fig. 1, 5b, black) may be produced in transient warming simulations (Fig. 5b, blue dotted line) through the combined effects of (i) the thermodynamic impact of a moist atmosphere on the sensitivity of effective horizontal diffusivity to temperature (Fig. 5a), and (ii) the impact of the Southern Ocean location of upwelling of water from the large heat-capacity deep ocean into the surface climate layer (Fig. 9).

6. Discussion

This study has presented three conceptual Energy Balance Models (EBMs) to explore possible explanations for the variation in surface warming of climate with latitude over the last century (Fig. 1, black); with greatest warming at high northern latitudes (Arctic Amplification) and reduced warming around 60° S. First, observations were used to develop new closures for longwave and shortwave radiation balances with temperature, latitude and cloudiness in the EBMs. The EBMs were then forced with imposed cloudiness and initial horizontal diffusivity fields and perturbed by radiative forcing to simulate the warming response with latitude.

6.1. Development of EBM closures

Many previous EBMs rely on relatively simple model closures to produce analytical solutions or approximations for surface temperature with latitude (e.g. [7,8], [9,11]). Here, instead observational fields were used to develop new closures for how outgoing longwave and shortwave radiation are affected by surface temperature, cloudiness and latitude. Key findings that were utilised in the EBMs were:

(i) The emissivity for outgoing longwave radiation is reduced by a factor of 1.38 for a cloudy sky relative to a clear sky, and this reduction scales with cloud amount (Fig. 2 g; Eqs. (13), (14)), while clear sky emissivity shows a good linear fit to surface temperature (Fig. 3; Eq. (21)).

(ii) The zonal- and annual-mean albedo of clouds with latitude was analysed from observational reconstructions of clear sky albedo, cloudy sky albedo and cloudiness (Fig. 2h, black; Eqs. (17), (22)), and found to be well approximated by a Legendre polynomial in sine of latitude with only one free parameter: the planetary mean albedo for clouds (Eq. (22); Fig. 2h, compare grey to black). This single free parameter finding is generalised in the EBM as a suitable approximation for the albedo variation in latitude for any surface (Eq. (21)), and used to develop a closure for clear sky albedo with temperature and latitude (Fig. 4; Eq. (21)). This enables all sky albedo to be calculated in the EBM based on surface temperature, latitude and cloudiness (Eqs. (15)–(22)).

By separating the impacts of latitude, temperature and cloudiness for both longwave and shortwave radiation budgets consistently with observations, the closures adopted allow the EBM to simulate the temperature response to perturbation in a different way to models that use simpler functions. Confidence is given to the application of these new closures because the simulated global-mean warming following a uniform radiative forcing of 3.71 Wm^{-2} (3.04 and 3.06 K for EBMs 1 and 2: Fig. 5c) is a similar order of magnitude to the current estimated range for the equilibrium climate sensitivity for the real climate system of 2.0 to 5.0 K [1], although note that the cloud amount does not vary in the EBM but cloud variation does contribute to the climate sensitivity in the real climate system.

6.2. Application of EBM to the causes of arctic amplification

Many possible explanations for Arctic Amplification of climate change have been proposed (e.g. [5,6], [33]). One possible explanation for Arctic amplification of surface warming is that local radiative feedbacks (for example reductions in surface albedo due to melting cryosphere) reduce the magnitude of the local 'climate feedback' ($\frac{\partial R_{out}}{\partial T_S}(\phi)$; Fig. 5d), and so a greater warming response is required to re-balance an imposed radiative forcing (e.g. [5,6]). This local radiative climate feedback effect is present in all EBM variants (Fig. 5d), but does not produce significant polar amplification in the first EBM variant where the effective horizontal diffusivity remains constant. The lack of this signal is because at high latitudes much of the radiative forcing is re-balanced by a change in divergence of the horizontal heat transport, rather than a vertical outgoing radiation response (Eq. (8)). Indeed, the outgoing radiation response with latitude is similar in all radiatively forced simulations (Fig. 5f), and these are also similar to the initial model state.

Another possible explanation for Arctic amplification is that changes in poleward heat transport preferentially heat the Arctic (e.g. [5]). However, in the conceptual EBM the poleward heat transport is only subtly altered between the initial perturbed states (Fig. 5e), the model variants with large Arctic Amplification do not appear significantly different in terms of poleward heat transport than the model variants without large Arctic Amplification.

The magnitude of observed high-northern latitude (Arctic) amplification of surface warming, relative to equatorial regions, is explained in the second and third EBM variants presented here (Fig. 5b, compare red and blue to black) by the way the Clausius–Clapeyron relation alters the ratio of poleward heat transport due to dry-static heat compared to latent heat. Assuming a constant relative humidity is retained, the fraction of heat transported in moving air via latent heat increases with surface warming (Eqs. (27)–(33)), while the fraction transported via dry heat reduces with surface warming. Therefore, the very similar heat transport is achieved with a lower equator-to-pole dry-bulb temperature gradient when temperatures are generally warmer, and more warming occurs at high latitudes to reduce the latitudinal temperature gradient.

The real world warming over the last century sees both enhanced relative warming at Northern high latitudes and reduced relative warming at around 60° South (Fig. 1, black). Neither the latitudinal variation in 'climate feedback' (Fig. 5d), nor the effective diffusivity sensitivity to warming (Fig. 5a), are able to produce both these features in the conceptual EBM (Fig. 5, compare red and grey to black). Instead, simulated warming is enhanced in both hemispheres at high latitudes.

The active surface climate system, comprising the atmosphere and surface ocean mixed layer, has a much smaller heat capacity than the deep ocean, and therefore responds thermally much faster to elevated greenhouse gas concentrations in the atmosphere. The delay in the temperature response of the deep ocean to radiative forcing then causes a non-zero global net heat flux between the surface ocean mixed layer and the deep ocean due to exchanges of water between the surface and deep regions. As the system is warmed from above radiatively, the downwelling water is warmer than the upwelling water, and so the deep ocean is warmed by the exchange while the surface ocean is cooled.

The cooling effect of the deep ocean on the surface ocean is not uniform with latitude, since over 60% of water in the deep ocean makes next contact with the surface mixed layer at high Southern latitudes in the Southern Ocean [29]. The third conceptual EBM variant presented here illustrates how this localised upwelling of water from the high heat capacity deep ocean effect, combined with temperature-sensitive diffusivity, can lead to both enhanced warming at high Northern latitudes and reduced warming over the Southern Ocean, in line with the observed pattern (Fig. 5b, compare blue dotted lines to black).

It should be noted that the explanations illustrated here, while being plausible, are not unique in being able to explain the observed warming pattern with latitude. For example, there could be dynamical explanations that also give rise to the observed latitudinal warming patterns that are not captured by the conceptual EBMs. These dynamical explanations are beyond the scope of the conceptual EBM presented here.

Declaration of competing interest

The authors declare that they have no known competing financial interests or personal relationships that could have appeared to influence the work reported in this paper.

Data availability

Model code for the three conceptual Energy Balance Models is available in the Matlab programming language (https://doi.org/10.5281/zenodo.8151916).

For absolute surface temperature record, T_S in K, the CRUTEM 5° by 5° absolute temperature dataset is used, giving from climatological monthly mean absolute surface temperatures from 1961–1990 ([14]: https://crudata.uea.ac.uk/cru/data/temperature/, downloaded 15–03–2022). When calculating $T_S^4(\phi)$ (Fig. 2a, red) the local temperatures are raised to the fourth power before zonal averaging.

For the surface temperature anomaly from 1900–1920 to 2000–2020 (Figs. 1, 5b) the HadCRUT5, version HadCRUT.5.0.1.0, was used ([2]: https://www.metoffice.gov.uk/hadobs/hadcrut5/data/current/download.html, downloaded 31-10-2022).

For outgoing radiation budgets, the CERES EBAF Edition 4.1 satellite observational dataset is used ([15]: https://ceres.larc.nasa.gov/data/, downloaded March 14th 2022), giving climatological mean values from the period July 2005 to June 2015. Here, zonal averages are extracted from the CERES dataset at 5°-latitude resolution, to match the resolution of the absolute temperature record, giving annual and zonal mean outgoing radiation under all sky and clear sky conditions for longwave, $L_{out,AllSky}(\phi)$ and $L_{out,ClearSky}(\phi)$ respectively (Fig 2a), and shortwave, $S_{out,AllSky}(\phi)$ and $S_{out,ClearSky}(\phi)$ (Fig. 2b).

For cloud amount fraction, f_{CA}, the CLARA v2.1 dataset was used [16,34]: Copernicus Climate Change Service [34], accessed on 10–01–2023, https://doi.org/10.24381/cds.68653055. The dataset is used here to calculate monthly climatological means for the period July 2005 to June 2015. Here, a 5° resolution for f_{CA} is extracted from the 0.25° resolution dataset to match the resolution of the absolute temperature dataset (Fig. 2e, showing annual- and zonal-mean f_{CA}).

Acknowledgements

The authors acknowledge UK NERC grant NE/T010657/1 and NE/T007788/1.

References

[1] P. Forster, T. Storelvmo, K. Armour, W. Collins, J.-L. Dufresne, D. Frame, D.J. Lunt, T. Mauritsen, M.D. Palmer, M. Watanabe, M. Wild, H. Zhang, The earth's energy budget, climate feedbacks, and climate sensitivity, in: V. Masson-Delmotte, P. Zhai, A. Pirani, S.L. Connors, C. Péan, S. Berger, N. Caud, Y. Chen, L. Goldfarb, M.I. Gomis, M. Huang, K. Leitzell, E. Lonnoy, J.B.R. Matthews, T.K. Maycock, T. Waterfield, O. Yelekçi, R. Yu, B. Zhou (Eds.), Climate Change 2021: The Physical Science Basis. Contribution of Working Group I To the Sixth Assessment Report of the Intergovernmental Panel on Climate Change, Cambridge University Press, Cambridge, United Kingdom and New York, NY, USA, 2021, pp. 923–1054, http://dx.doi.org/10.1017/9781009157896.009.

[2] C.P. Morice, J.J. Kennedy, N.A. Rayner, J.P. Winn, E. Hogan, R.E. Killick, R.J.H. Dunn, T.J. Osborn, P.D. Jones, I.R. Simpson, An updated assessment of near-surface temperature change from 1850: the HadCRUT5 data set, J. Geophys. Res.: Atmos. 126 (2021) e2019JD032361, http://dx.doi.org/10.1029/2019JD032361.

[3] J.D. Annan, J.C. Hargreaves, T. Mauritsen, A new global surface temperature reconstruction for the last glacial maximum, Clim. Past 18 (2022) 1883–1896, http://dx.doi.org/10.5194/cp-18-1883-2022.

[4] J.E. Tierney, J. Zhu, M. Li, A. Ridgwell, G.J. Hakim, C.J. Poulsen, R.D.M. Whiteford, J.W.B. Rae, L.R. Kump, Spatial patterns of climate change across the paleocene-eocene thermal maximum, Proc. Natl. Acad. Sci. USA 119 (42) (2022) http://dx.doi.org/10.1073/pnas.2205326119.

[5] M. Previdi, K.L. Smith, L.M. Polvani, Arctic amplification of climate change: a review of underlying mechanisms, Environ. Res. Lett. 16 (9) (2021) 093003, http://dx.doi.org/10.1088/1748-9326/ac1c29.

[6] P.C. Taylor, M. Cai, A. Hu, J. Meehl, W. Washington, G.J. Zhang, A decomposition of feedback contributions to polar warming amplification, J. Clim. 26 (18) (2013) 7023–7043, http://dx.doi.org/10.1175/JCLI-D-12-00696.1.

[7] M.I. Budyko, The effect of solar radiation variations on the climate of the earth, Tellus 21 (1969) 611–619.

[8] G.R. North, Theory of energy-balance climate models, J. Atmos. Sci. 32 (11) (1975) 2033–2043, http://dx.doi.org/10.1175/1520-0469(1975)032<2033:TOEBCM>2.0.CO;2.

[9] T.M. Merlis, M. Henry, Simple estimates of polar amplification in moist diffusive energy balance models, J. Clim. 31 (2018) 5811–5824, http://dx.doi.org/10.1175/JCLI-D-17-0578.1.

[10] R.T. Pierrehumbert, Principles of Planetary Climate, Cambridge University Press, Cambridge, UK, ISBN: 978-0-521-86556-2, 2010, p. 652.

[11] W. Sellers, A climate model based on the energy balance of the earth-atmosphere system, J. Appl. Meteorol. 8 (1969) 392–400.

[12] G.R. North, R.F. Cahalan, J.A. Coakley Jr., Energy balance climate models, Rev. Geophys. Space Phys. 19 (1) (1981) 91–121, http://dx.doi.org/10.1029/RG019i001p00091.

[13] J.M. Gregory, Vertical heat transports in the ocean and their effect on time-dependent climate change, Clim. Dynam. 16 (2000) 501–515, http://dx.doi.org/10.1007/s003820000059.

[14] P.D. Jones, M. New, D.E. Parker, S. Martin, I.G. Rigor, Surface air temperature and its variations over the last 150 years, Rev. Geophys. 37 (1999) 173–199, http://dx.doi.org/10.1029/1999RG900002.

[15] N.G. Loeb, D.R. Doelling, H. Wang, W. Su, C. Nguyen, J.G. Corbett, L. Liang, C. Mitrescu, F.G. Rose, S. Kato, Clouds and the earth's radiant energy system (CERES) energy balanced and filled (EBAF) top-of-atmosphere (TOA) edition-4.0 data product, J. Clim. 31 (2) (2018) 895–918, http://dx.doi.org/10.1175/JCLI-D-17-0208.1.

[16] K.-G. Karlsson, A. Riihelä, J. Trentmann, M. Stengel, J.F. Meirink, I. Solodovnik, A. Devasthale, T. Manninen, E. Jääskeläinen, K. Anttila, V. Kallio-Myers, N. Benas, N. Selbach, D. Stein, J. Kaiser, R. Hollmann, ICDR AVHRR - based on CLARA-A2 methods, Satell. Appl. Facil. Clim. Monit. (2021) http://dx.doi.org/10.5676/EUM_SAF_CM/CLARA_AVHRR/V002_01.

[17] S.C. Sherwood, M.J. Webb, J.D. Annan, K.C. Armour, P.M. Forster, J.C. Hargreaves, et al., An assessment of Earth's climate sensitivity using multiple lines of evidence, Rev. Geophys. 58 (2020) e2019RG000678, http://dx.doi.org/10.1029/2019RG000678.

[18] D.D.B. Koll, T.W. Cronin, Earth's outgoing longwave radiation linear due to H_2O greenhouse effect, Proc. Natl. Acad. Sci. 115 (41) (2018) 10293–10298, http://dx.doi.org/10.1073/pnas.1809868115.

[19] D.L. Hartmann, Global Physical Climatology, Academic Press, San Diego, USA, ISBN: 0-12-328530-5, 1994, p. 411.

[20] M. Wild, D. Folini, M.Z. Hakuba, C. Schär, S.I. Seneviratne, S. Kato, D. Rutan, C. Ammann, E.F. Wood, G. König-Langlo, The energy balance over land and oceans: an assessment based on direct observations and CMIP5 climate models, Clim. Dynam. 44 (11) (2015) 3393–3429.

[21] M.D. Shupe, J.M. Intrieri, Cloud radiative forcing of the Arctic surface: The influence of cloud properties, surface albedo, and solar zenith angle, J. Clim. 17 (3) (2004) 616–628.

[22] C.M. Bitz, G.H. Roe, A mechanism for the high rate of sea ice thinning in the arctic ocean, J. Clim. 17 (2004) 3623–3632, http://dx.doi.org/10.1175/1520-0442(2004)017<3623:AMFTHR>2.0.CO;2.

[23] C.E. Graves, W.-H. Lee, G.R. North, New parameterizations and sensitivities for simple climate models, J. Geophys. Res. 98 (D3) (1993) 5025–5036, http://dx.doi.org/10.1029/92JD02666.

[24] P.H. Stone, Constraints on dynamical transports of energy on a spherical planet, Dyn. Atmos. Oceans 2 (2) (1978) 123–139, http://dx.doi.org/10.1016/0377-0265(78)90006-4.

[25] I.M. Held, M.J. Suarez, Simple albedo feedback models of the icecaps, Tellus 26 (6) (1974) 613–629, http://dx.doi.org/10.3402/tellusa.v26i6.9870.

[26] R.S. Lindzen, B. Farrell, Some realistic modifications of simple climate models, J. Atmos. Sci. 34 (1977) 1487–1501, http://dx.doi.org/10.1175/1520-0469(1977)034<1487:SRMOSC>2.0.CO;2.

[27] Y. Huang, X. Tan, Y. Xia, Inhomogeneous radiative forcing of homogeneous greenhouse gases, J. Geophys. Res.: Atmos. 121 (2016) 2780–2789, http://dx.doi.org/10.1002/2015JD024569.

[28] N. Feldl, T.M. Merlis, Polar amplification in idealized climates: The role of ice, moisture, and seasons, Geophys. Res. Lett. 48 (2021) e2021GL094130, http://dx.doi.org/10.1029/2021GL094130.

[29] T. DeVries, F. Primeau, Dynamically and observationally constrained estimates of water-mass distributions and ages in the global ocean, J. Phys. Oceanogr. 41 (2011) 2381–2401, http://dx.doi.org/10.1175/JPO-D-10-05011.1.

[30] E. Beer, I. Eisenman, T.J.W. Wagner, Polar amplification due to enhanced heat flux across the halocline, Geophys. Res. Lett. 47 (2020) e2019GL086706, http://dx.doi.org/10.1029/2019GL086706.

[31] E. Beer, I. Eisenman, T.J.W. Wagner, E.C. Fine, A possible hysteresis in the Arctic ocean due to release of subsurface heat during sea ice retreat, J. Phys. Oceanogr. 53 (2023) 1323–1335, http://dx.doi.org/10.1175/JPO-D-22-0131.1.

[32] S.A. Hill, N.J. Burls, T.M. Merlis, Symmetric and antisymmetric components of polar-amplified warming, J. Clim. 35 (2022) 6757–6772, http://dx.doi.org/10.1175/JCLI-D-20-0972.1.

[33] M. Jenkins, A. Dai, The impact of sea-ice loss on Arctic climate feedbacks and their role for Arctic amplification, Geophys. Res. Lett. 48 (2021) e2021GL094599, http://dx.doi.org/10.1029/2021GL094599.

[34] Copernicus Climate Change Service (C3S), Cloud properties global gridded monthly and daily data from 1982 to present derived from satellite observations, Copernicus Climate Change Service (C3S) Climate Data Store (CDS), 2022, http://dx.doi.org/10.24381/cds.68653055 (Accessed 10 January 2023).